Title

Organometallic uranyl complexes for photocatalytic C-H bond activation and functionalization

Permalink

Author

Rutkauskaite, Ryte

Publication Date

2023

Organometallic uranyl complexes for photocatalytic C-H bond activation and functionalization

By

Ryte Rutkauskaite

A dissertation submitted in partial satisfaction of the
requirements for the degree of
Doctor of Philosophy
in
Chemistry
in the
Graduate Division
of the
University of California, Berkeley

Committee in charge:
Professor Polly L. Arnold, Chair
Professor Thomas J. Maimone
Professor Yury G. Kolomensky

Summer 2023

Abstract

Organometallic uranyl complexes for photocatalytic C-H bond activation and functionalization

by

Ryte Rutkauskaite

Doctor of Philosophy in Chemistry

University of California, Berkeley

Professor Polly L. Arnold, Chair

Chapter one discusses the synthesis and characterization of novel complexes of the uranyl(VI) ion with a substituted phenanthroline ligand ph_2phen. The complexes are investigated by electronic and vibrational spectra and their solid-state structures are presented. Luminescence spectra and lifetimes are determined. Density functional theory (DFT) calculations are carried out to investigate the electronic structure of the complexes in the ground and excited states.

Chapter two discusses the photocatalytic reactivity of the new uranyl complexes in alkane fluorination, oxidation and C-C coupling reactions. Visible light mediated functionalization of the C-H bond in the substrate is achieved through hydrogen atom abstraction. The identity of the photocatalyst is investigated for the fluorination reactions. DFT calculations are performed to compare reaction energy barriers for different photocatalysts and gauge the interactions between the substrate and ph_2phen ligand. Finally, Stern-Volmer analyses are performed to determine the nature of collisional quenching between the substrate and the photocatalyst.

Lay Summary

Uranium is the heaviest naturally occurring element found both in rocks and sea water. While it is probably best known for its use in nuclear energy and nuclear weapons, less than 1% of natural uranium is the isotope used for these purposes (U-235), with the majority (over 99%) being the less radioactive U-238 isotope.

The most common chemical form of uranium in the environment is the uranyl ion, $[UO_2]^{2+}$. A unique property of this species is that, when exposed to purple- or blue-colored light, it becomes chemically reactive. One of the reactions facilitated by the uranyl ion is C-H bond abstraction, wherein uranyl breaks the carbon-hydrogen bond in an organic molecule, binding the hydrogen atom. C-H bonds in organic compounds are relatively strong, and the ability to cleave them without otherwise decomposing the molecule is of great interest to synthetic chemists. After performing C-H bond abstraction, the uranyl ion can be regenerated, making these reactions (photo)catalytic.

While the field of photocatalysis has been quickly growing in recent years, most studies have focused on transition metal catalysts. In the reports that do focus on uranyl photocatalysis, simple salts such as uranyl nitrate or uranyl acetate have almost exclusively been tested, and the reactivity of more complicated uranyl compounds has not been explored. This thesis reports the synthesis of novel uranyl-containing molecules and studies their light-absorbing properties and photocatalytic behavior.

In memory of Luca

Table of contents

Chapter 1: Synthesis and characterization of new organometallic uranyl photocatalysts

Chapter 2: Photocatalytic C-H bond functionalization by phenanthroline-based uranyl complexes

Acknowledgements

I would like to thank Polly Arnold for the opportunity to come to Berkeley and experience doing research here. To the whole Parnold group, I could not have asked for a better team to work with. To Amy Kynman, I am so proud of us for powering through these crazy few years. From setting up an empty lab to Christmas in quarantine to writing our theses in the library together, having you with me made it all easier. To Francis Lam, thank you for our hikes and being one of my first ever climbing partners. To Gabe Herrera, our lunches together have kept me sane in the past year. You are an amazing scientist and I know that our subgroup is in great hands. To Amy Price, Rachel Meyer, Mikaela Pyrch, Elias Tanuhadi, Anthony Wong and Addison Desnoyer, thank you for all your help in the lab and beyond, time and time again I was so impressed by how much knowledge you can all fit in your brains. To Jamie Purkis, for your kind support and establishing the uranyl photocatalysis project in the group. To Yanlin Liu, it was a pleasure to mentor you and I look forward to seeing everything you achieve in the future. To Matt Hernandez, you and Skye always remind me what it feels like to laugh until my stomach hurts. To Nick Katzer, thanks for being another one of my original climbing buddies and sharing your encyclopedic knowledge with the group. To Gretchen Brown, David Fiszbein, Michael Trinh, Jaden Lara and Mary Johnson, thank you for all the laughs in the office and after work.

To Luca Elghanayan, it was a privilege to know you and to work alongside you. Thank you for listening to music in the lab with me, for the Dogpatch weekends with the group, for the chats on the way to and back from Tahoe. I hope to one day be half as kind as you were to everyone around you. We miss you so much.

To our collaborators Louise Natrajan, Adam Woodward, Xiaobin Zhang and Georg Schreckenbach – it was lovely to work with you and thank you for your patience with me while I was navigating this PhD.

Thank you to Anneke Runtupalit and Angela Green for helping our group run. To Hasan Celik and Elena Kreimer for supporting the research of so many of us in the Chemistry Department.

Thank you to John Arnold, Jade Fostvedt, Rex Handford, Erik Ouelette, Chris Ye, Joe Brackbill, Harry Bergman and Michael Boreen for the camping trips and for helping our group out so much when we first started in Berkeley. To Jacob Branson for our trips to Marin and looking at rocks with me. To Sheridon Kelly for our boba breaks and not talking about science.

To Max Gallant, I could not have done this without you. Thanks for showing me that running uphill is not that bad, especially when there are good views and even better company involved. I am forever thankful.

To my mum, grannies, and the rest of my family, thank you for your love and for supporting everything I choose to do. To friends at home, in Berkeley and everywhere in between, I am so lucky to have you in my life.

Chapter 1

Synthesis and characterization of new organometallic uranyl photocatalysts

1.1 Overview

The aqueous uranyl dication has long been known to facilitate hydrogen atom abstraction from organic substrates *via* the long-lived highly efficient excited state, yet the use of additional ligands to control this reactivity has barely been explored. This chapter discusses the synthesis and characterization of novel uranyl chloride photocatalysts with the 4,7-diphenyl-1,10-phenanthroline ligand. Luminescence spectra and excited state lifetimes of the compounds are measured to gain insight into their photoreactivity. DFT calculations of excitation energies and excited-state spin density of the complexes are discussed as well.

Luminescence spectroscopy and excited state lifetime measurements discussed in this chapter were performed by Dr. Adam Woodward and Dr. Louise Natrajan at the University of Manchester and National Nuclear User Facility in the United Kingdom. The computational work was done by Dr. Xiaobin Zhang and Prof. Georg Schreckenbach at the University of Manitoba, Canada. Support for the synthetic work was provided by the Office of Science, Office of Basic Energy Sciences, Division of Chemical Sciences, Geosciences, and Biosciences Heavy Elements Chemistry program of the U.S. Department of Energy under Contract Number DE-AC02-05CH11231 at LBNL.

1.2 Introduction

The uranyl dication (Figure 1.1) is the predominant form of uranium in the environment with a rigidly linear and chemically stable $[O\equiv U\equiv O]^{2+}$ moiety. The triple oxygen-uranium bonds, by convention commonly noted as U=O, arise from overlap of oxygen 2*p* orbitals and a hybrid state of the 5*f* and 6*d* orbitals on uranium, resulting in one π- and two σ-bonds. This U(VI), f^0 species absorbs visible light of *ca.* 400 nm, in most cases giving uranyl complexes their characteristic yellow color. This absorption induces a ligand to metal charge transfer (LMCT) from a bonding oxygen orbital to a non-bonding uranium orbital, formally yielding a U(V) oxyl radical species. The excited species fluoresces at *ca.* 520 nm with excited state lifetimes often in the range of microseconds.[1] This excited state fluorescence can be quenched by multiple processes, including hydrogen atom abstraction (HAA) from organic substrates such as alcohols and unactivated hydrocarbons.[2] The reactivity of the uranyl ion is further discussed in Chapter 2.

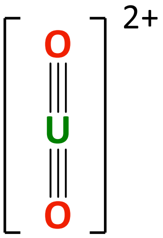

Figure 1.1 The uranyl dication, $[UO_2]^{2+}$. Bonds denoting equatorial ligands (those in the plane perpendicular to the *trans*-dioxo uranyl unit) are omitted for clarity.

Fluorescence properties of uranyl complexes have been explored since the Manhattan project and the first studies of uranyl photocatalysis date back to the 1970s. While the focus in the field has been on fluorescence and reactivity of the species in aqueous conditions, uranyl photocatalysis in organic solvents is relatively underexplored, and examples of uranyl photocatalysts that incorporate organic ligands in the equatorial position are even fewer.

In the recent years, 1,10-phenanthroline (phen) and its derivatives have been used ubiquitously in photocatalysis. Transition metal complexes containing phen have been explored as photocatalysts and photosensitizers for water splitting[3,4] as well as other types of photoredox reactions.[5,6] In addition, phen has been used with Ln(III) ions to synthesize intensely fluorescent molecules with potential applications in lighting and lasers.[7] In some cases, the antenna effect, *i.e.* sensitization of the emitting metal ion through efficient phen ligand absorption, followed by energy transfer, is accomplished. A uranyl phenanthroline cluster has recently been shown to have potential as a fluorometric UV and X-ray indicator.[8]

The first example of a molecular uranyl complex with the unsubstituted phen ligand was reported in the 1960s.[9] Uranyl nitrate was used as the starting material resulting in $UO_2(NO_3)_2$phen, with examples of *mono* phen complexes of uranyl chloride and sulfate reported slightly later.[910] Much more recently, an example of a *bis* phen uranyl chloride complex, $[UO_2Cl_2(phen)_2]$, was reported by Schoene *et al*. with the uranyl unit significantly bent at 161.8(1)°.[11] The phtotocatalytic properties of the *mono* or *bis* phen uranyl complexes were, however, not explored.

In 2019, our group reported the new uranyl-phenanthroline complex $[UO_2(NO_3)_2(ph_2phen)]$ **1-NO₃** (ph₂phen = 4,7-diphenyl-1,10-phenanthroline, Scheme 1.1) as a catalyst for the oxidation of benzylic C−H bonds as well as C−C bond cleavage in 2-phenoxy-1- phenylethanol (2P1PE), a model for the parts of lignin that are most challenging to cleave.[12] We found that **1-NO₃** gave higher conversions than uranyl nitrate for most substrates tested. Using the phenyl substituted ligand helped to better solubilize the complex in acetonitrile, the solvent of choice for the photocatalytic reactions, compared to unsubstituted phen complexes. Following this report, we aimed to expand the list of uranyl ph₂phen photocatalysts to analogous chloride complexes with one and two equivalents of ph₂phen coordinated.

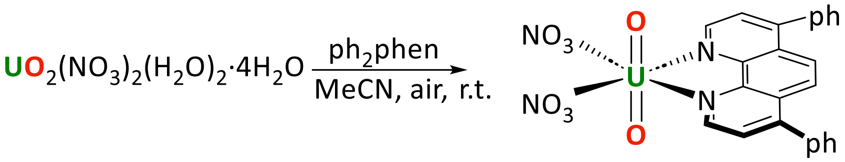

Scheme 1.1 Synthesis of **1-NO₃**.

1.3 Results and discussion

1.3.1 Synthesis and characterization of uranyl chloride ph2phen complexes

The syntheses of the acetonitrile adduct of uranyl dichloride as well as the *mono* and *bis* ph$_2$phen uranyl chloride complexes are shown in Scheme 1.2. Uranyl chloride acetonitrile solvate [UO_2Cl_2(MeCN)] is also synthesized as a water-free control complex for anaerobic photocatalysis reactions discussed in Chapter 2. While the complex contains one equivalent of MeCN in solid state, in acetonitrile solution it is presumed to form a *tris* MeCN complex [$UO_2Cl_2(MeCN)_3$], similar to the previously reported THF solvate [$UO_2Cl_2(THF)_3$].[13]

The complex **1-Cl-MeCN** can be made from the combination of equimolar ph$_2$phen and the pale-yellow uranyl chloride hydrate ([$UO_2Cl_2 \cdot 3H_2O$]) in acetonitrile, which forms a dark yellow solution. The subsequent removal of solvent under reduced pressure yields [UO_2Cl_2(ph$_2$phen)(MeCN)], **1-Cl-MeCN,** as an orange solid which is very soluble in acetonitrile and acetone. The ^{1}H NMR spectrum of a CD_3CN solution of the complex confirms the coordination of ligand, with resonances shifted as far as 2 ppm higher in frequency compared to free ligand, for example the two protons closest to the U(VI) center resonate at 11.27 ppm, compared to 9.17 in free ligand and 9.25 in protonated ligand. During the synthesis of **1-Cl-MeCN**, the formation of a small amount of a bright yellow solid, the less-soluble complex **2**, discussed below, is consistently observed. While single crystals of the acetonitrile adduct **1-Cl-MeCN** could not be isolated, vapor diffusion of hexanes into a THF solution of the crude solid yields crystals of [UO_2Cl_2(ph$_2$phen)(THF)], **1-Cl-THF**, while vapor diffusion of hexanes into a chlorobenzene solution affords the unsolvated dimer [UO_2Cl_2(ph$_2$phen)]$_2$, **[1-Cl]$_2$**.

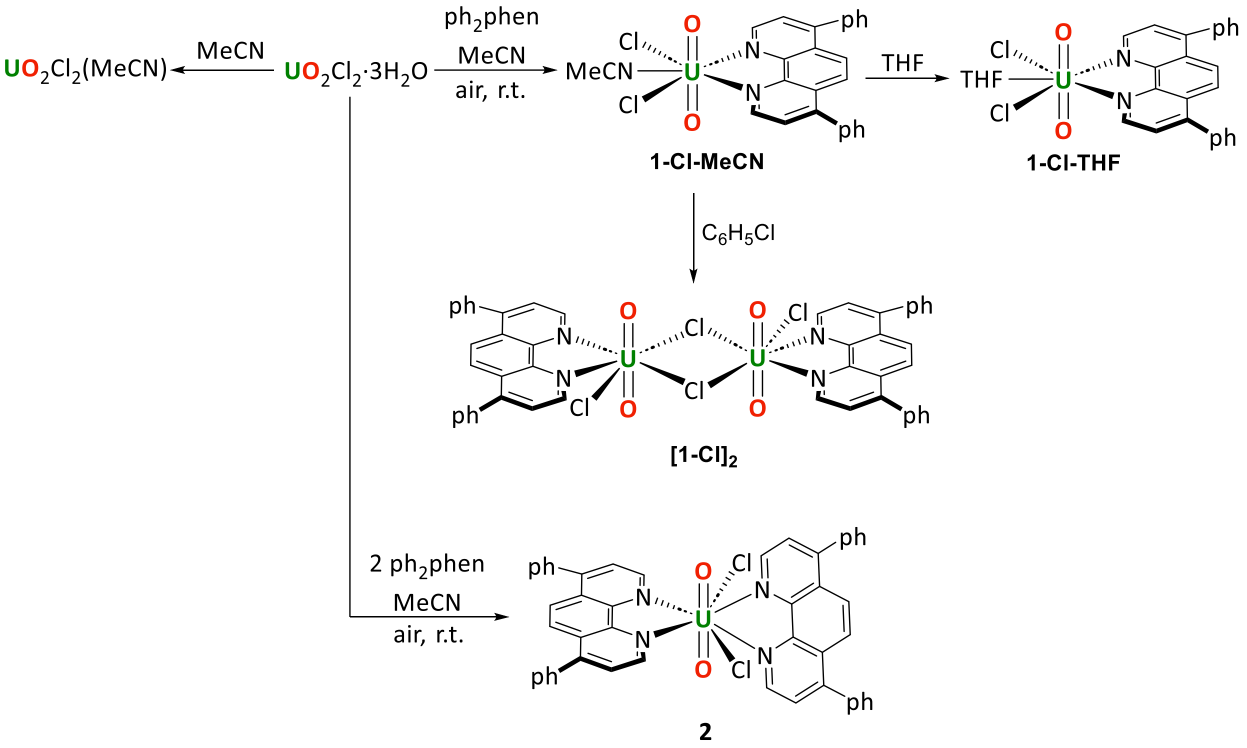

Scheme 1.2 Syntheses of complexes **1-Cl-MeCN**, **1-Cl-THF**, **[1-Cl]$_2$** and **2**.

The asymmetric U=O stretch in the IR spectrum of **1-Cl-MeCN** appears at 922 cm^{-1}, which is lower than that of the anhydrous uranyl chloride [UO_2Cl_2(MeCN)] (953 cm^{-1}), indicating that the U=O bond is weakened upon complexation of ph$_2$phen. The λ_{max} of the uranyl LMCT in the electronic absorption spectrum of **1-Cl-MeCN** in acetonitrile appears at 452 nm (ε = 56 M^{-1}cm^{-1}), which is red-shifted compared to uranyl chloride starting material (432 nm) and the nitrate analogue **1-NO$_3$** (427 nm), indicating that **1-Cl-MeCN** requires a lower energy to access the photoactive excited state.

The addition of an acetonitrile solution of uranyl chloride hydrate ([$UO_2Cl_2\cdot 3H_2O$]) to an acetonitrile solution of two equivalents of ph$_2$phen immediately results in the precipitation of a bright yellow powder characterized as [UO_2Cl_2(ph$_2$phen)$_2$] **2**, in 89% yield. **2** is almost completely insoluble in acetonitrile or acetone, and sparingly soluble in methanol, chloroform, or dichloromethane. The ^{1}H NMR spectrum of **2** in CD_3Cl solution shows ph$_2$phen resonances again shifted to around 1ppm higher frequency compared to free ph$_2$phen. In the IR spectrum of the complex, ν_{asym}(U=O) appears at 900 cm^{-1}, which shows that the U=O bond is significantly weakened compared to **1-Cl-MeCN** (925 cm^{-1}), but is similar to that in the previously reported [UO_2Cl_2(phen)$_2$] (898 cm^{-1}).[11]

The solid-state structures of all complexes were determined by single crystal X-ray diffraction at 100 K. Complex **1-Cl-THF** (Figure 1.2) crystallizes in a $P2_1/n$ space group with one molecule in the asymmetric unit. The uranium center is seven-coordinate with a pentagonal bipyramidal coordination geometry. The uranyl U-O$_{yl}$ bond distances are typical for uranyl complexes (1.763(2)

Å and 1.766(2) Å), as is the O_{yl}-U-O_{yl} angle (177.41(8)°). The U-Cl bonds (2.7023(7) and 2.7057(6) Å) are comparable to those in the previously reported uranyl chloride THF solvate $UO_2Cl_2(THF)_3$ (2.687(2) and 2.698(2) Å).[13] The U-N bond distances in **1-Cl-THF** are 2.627(2) and 2.639(2) Å, similar to those in the nitrate analogue **1-NO₃** (2.589(3) and 2.625(4) Å).[12] The ph₂phen ligand in **1-Cl-THF** is nearly perpendicular to the uranyl group (87.98° dihedral angle calculated between the plane of the uranyl unit and the plane of the ph₂phen backbone). In contrast, in **1-NO₃** and other eight-coordinate uranyl nitrate N-heterocyclic complexes with the 2,2′-bipyridyl (bipy) and unsubstituted phen ligand, the ligand is distorted from the equatorial plane by at least 20°, likely due to uranium center being more sterically crowded.[14,15]

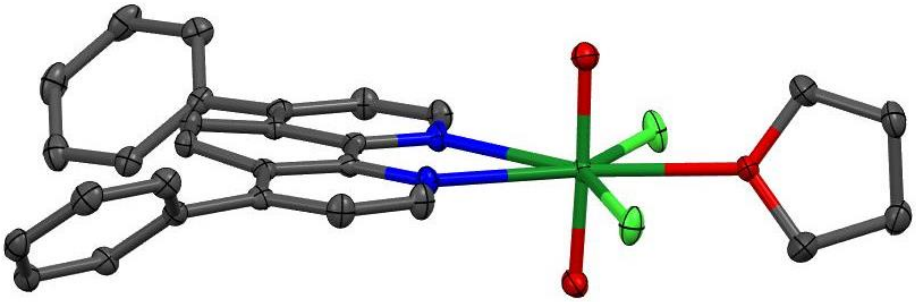

Figure 1.2 Solid-state structure of **1-Cl-THF** with thermal ellipsoids at the 50% probability level. Hydrogen atoms are omitted for clarity. Color code: dark green – U, red – O, light green – Cl, blue – N, grey - C.

The dimer **[1-Cl]₂** (Figure 1.3) crystallizes in a *C*2/*c* space group with half of the complex in the asymmetric unit. Each uranium atom is seven-coordinate in a pentagonal bipyramidal geometry. The uranyl U-O_{yl} bond distances (1.745(3) and 1.755(3) Å) and the O_{yl}-U-O_{yl} angle (178.1(1)°) are standard for uranyl complexes. The U-$Cl_{bridging}$ bond lengths are 2.768(1) and 2.793(1) Å, similar to those in the reported dimeric uranyl chloride THF solvate $[UO_2Cl_2(THF)_2]$ avg. 2.82 Å.[16] The U-N bond distances (2.562(3) and 2.621(3) Å) are comparable to those in **1-Cl-THF**, while the U-$Cl_{terminal}$ bond length is slightly shorter in the dimer **[1-Cl]₂** (2.644(1) Å).

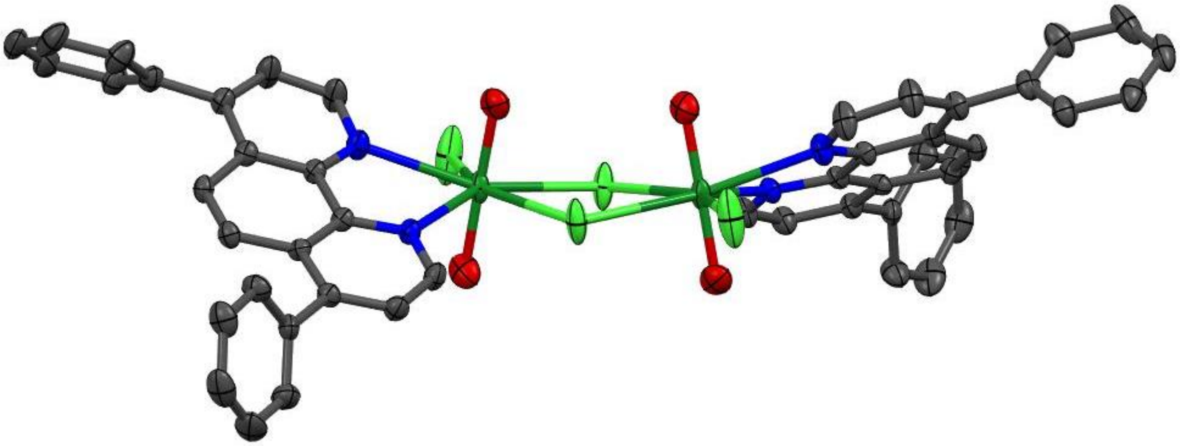

Figure 1.3 Solid-state structure of **[1-Cl]₂** with thermal ellipsoids at the 50% probability level. Hydrogen atoms and solvent molecules are omitted for clarity. Color code: dark green – U, red – O, light green – Cl, blue – N, grey - C.

The *bis* ph_2phen complex **2** (Figure 1.4) crystallizes in the $P2_12_12_1$ space group with one molecule in the asymmetric unit. The uranium center is eight-coordinate with a dodecadeltahedron coordination geometry. While the $U\text{-}O_{yl}$ bond distances are standard (1.777(2) and 1.777(3) Å), the uranyl unit is significantly bent (163.4(1)°), though slightly less so than in the reported analogue with unsubstituted phen, $[UO_2Cl_2(phen)_2]$ (161.8(1)°). One of the ph_2phen ligands in **2** is in the equatorial plane, while the other is closer aligned to the axial UO_2 group. The U-N bonds are shorter with ph_2phen in the equatorial position compared to axial (2.615(3) and 2.662(4) *vs.* 2.782(3) and 2.816(3) Å). The U-Cl bond distances (2.684(1) and 2.688(1) Å) are slightly shorter than in **1-Cl-THF**.

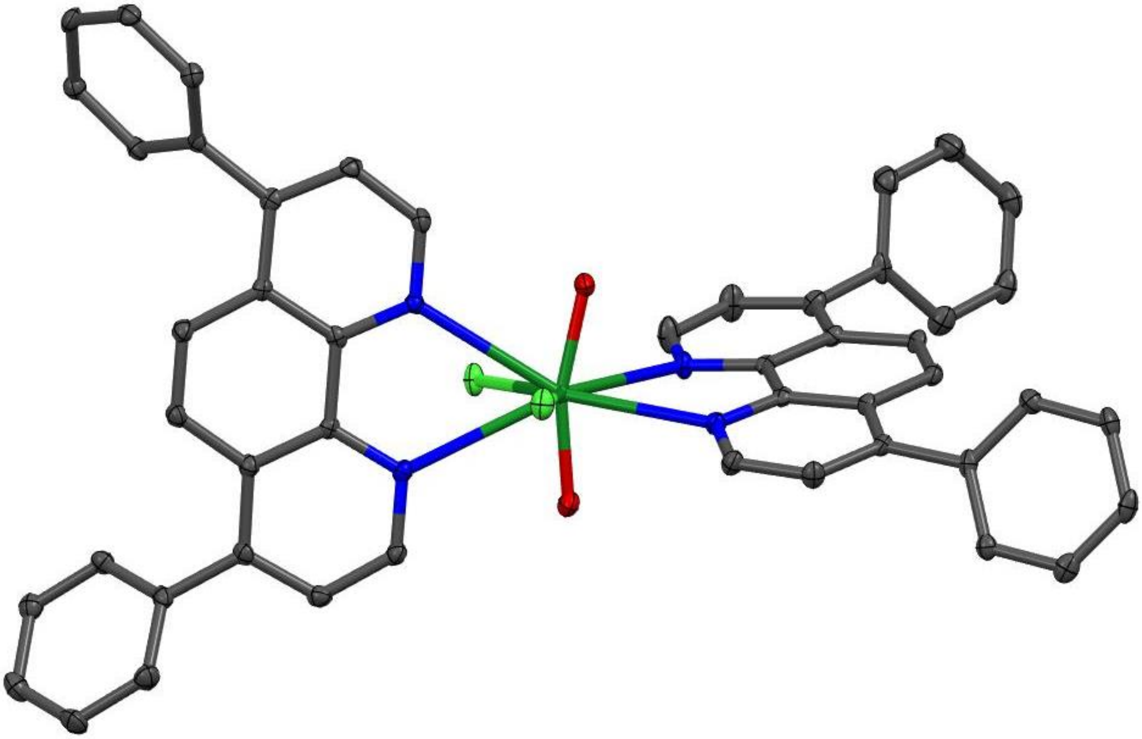

Figure 1.4 Solid-state structure of **2** with thermal ellipsoids at the 50% probability level. Hydrogen atoms are omitted for clarity. Color code: dark green – U, red – O, light green – Cl, blue – N, grey – C.

1.3.2 Luminescence spectroscopy

Steady state excitation and emission spectra were measured for ph$_2$phen ligand, the previously reported uranyl nitrate ph$_2$phen complex **1-NO$_3$**, and the new chloride complexes **1-Cl-MeCN** and **2**. Luminescence lifetimes were also measured for the compounds as well as uranyl nitrate ($[UO_2(NO_3)_2(H_2O)_2]$) and uranyl chloride acetonitrile adduct ($[UO_2Cl_2(MeCN)]$) for comparison.

The absorbance, excitation, and emission spectrum of the ph$_2$phen ligand in acetonitrile (Figure 1.5, left) show consistent absorption and emission maxima at 273 nm and 380 nm respectively. Upon excitation into the absorption bands at 272 nm, ph$_2$phen exhibits fluorescence with a maximum at 380 nm. The excitation spectra produced when monitoring the central emission wavelength show good agreement with the absorption spectra. When repeating the measurements in frozen 2-methyl tetrahydrofuran (Me-THF) glass (Figure 1.5, right) the fluorescence emission band becomes resolved, with peaks at 356, 375, and 393 nm. Similar vibrationally resolved emission is also recorded with maxima at 476, 511, and 550 nm. The excitation spectra recorded by monitoring the emission at each of these maxima are superimposable, which indicates that the longer wavelength emission is phosphorescence.[7]

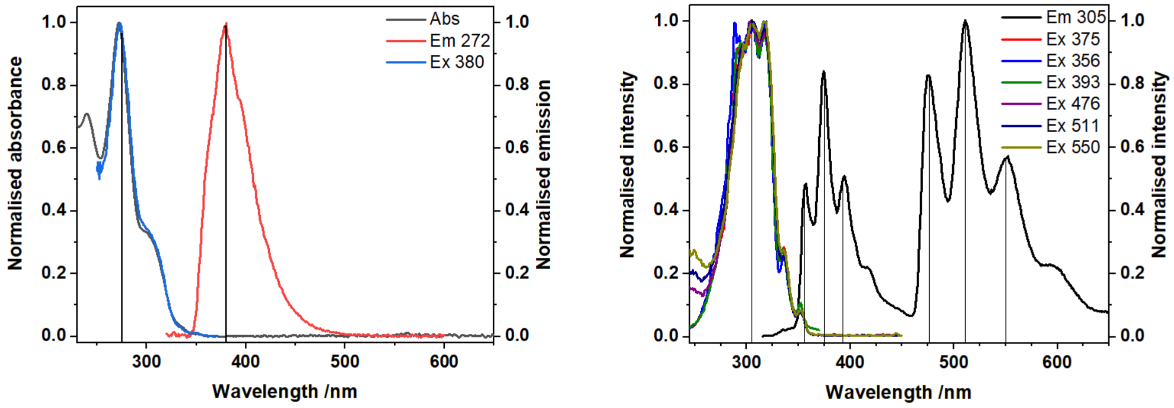

Figure 1.5 Left: absorption (black line), emission (red), and excitation (blue) spectra of ph_2phen ligand in MeCN. Right: low temperature (77 K) emission (red) and excitation (blue) spectra of ph_2phen ligand in frozen Me-THF.

Time resolved measurements of the ph_2phen ligand at 77 K (Figure 1.6) support the assignment of the *ca.* 510 nm emission band being phosphorescence as the lifetime of ~5.1 μs is substantially longer than the *ca.* 393 nm emission band (~2.8 μs).

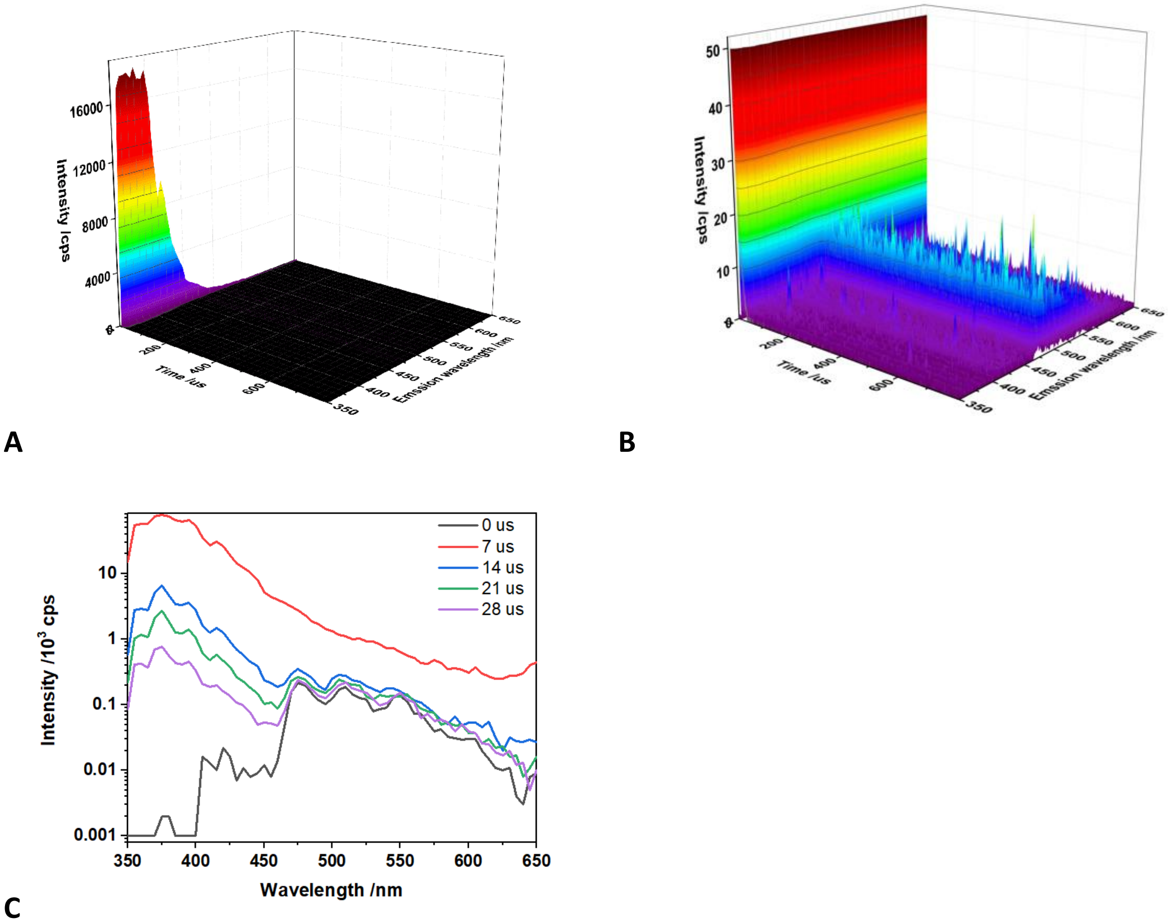

Figure 1.6 Low temperature (77 K) time resolved emission spectra map (A, expanded B) and time sliced spectra (C) of ph$_2$phen in frozen Me-THF showing the short lived and longer-lived emission bands are fluorescence and phosphorescence respectively. λ_{ex} = 305 nm.

The complexation of a single ph$_2$phen ligand with uranyl(VI) to afford **1-NO$_3$** leads to a shoulder on the low energy side of the absorption envelope (350 – 400 nm), likely due to the uranyl charge transfer (Figure 1.7, left). In the room temperature spectrum recorded in MeCN, two convoluted emission bands are observed at 445 nm and 520 nm; the lower energy band displaying the well-known fine structure arising from vibronic coupling in the uranyl moiety. This is confirmed through the use of gated detection, where the short wavelength side of the emission band drops away with a 50 µs gate (blue trace in Figure 1.7, left), revealing more detail on the signal from the uranyl LMCT emission. Low temperature (77 K) studies (Figure 1.7, right) yield more resolution of the uranyl emission fine structure and a significant reduction in the relative intensity of the 445 nm feature which is indicative of the suppression of thermally activated back energy transfer processes that lead to population of a close lying LMCT state. These observations alongside previous works lead to the assignment of the emission band centered at 445 m, as ph$_2$phen ligand to uranium charge transfer and at lower energy (520, 540 nm), oxygen to uranium LMCT, respectively.[17] Indeed, the excitation spectra of these bands show some vibrational fine structure as commonly observed in uranyl-based charge transfer excitations.[18]

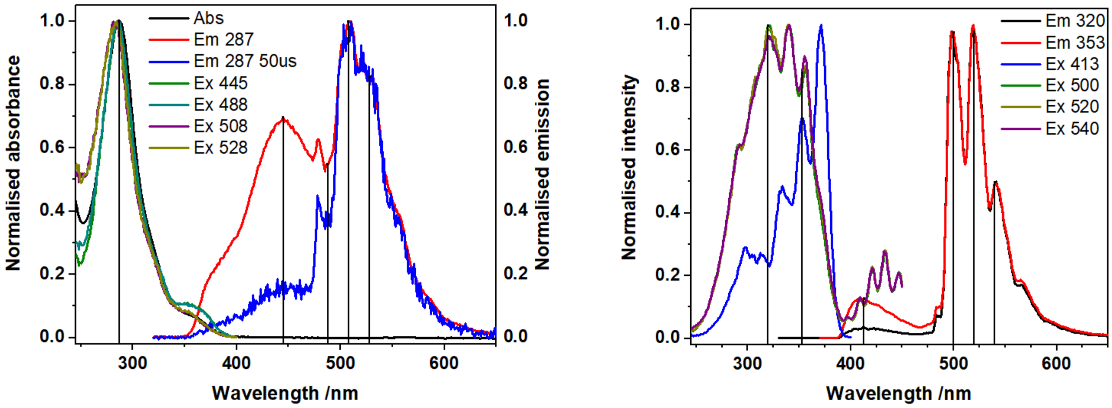

Figure 1.7 Left: absorption, emission, and excitation spectra of **1-NO₃** in acetonitrile at room temperature. Right: low temperature (77 K) emission and excitation spectra of **1-NO₃** in frozen MeTHF.

Time resolved measurements of room temperature MeCN solutions of **1-NO₃** (Figure 1.8) show that the uranyl emission is much longer lived (4.68 (20%) and 13.9 µs (80%) for the 528 nm band) than the equatorial LMCT emission, which has decayed to near background intensity after 30 microseconds. In frozen solution at 77 K in Me-THF, the uranyl emission possesses a lifetime of ~185 µs (Figure 1.9).

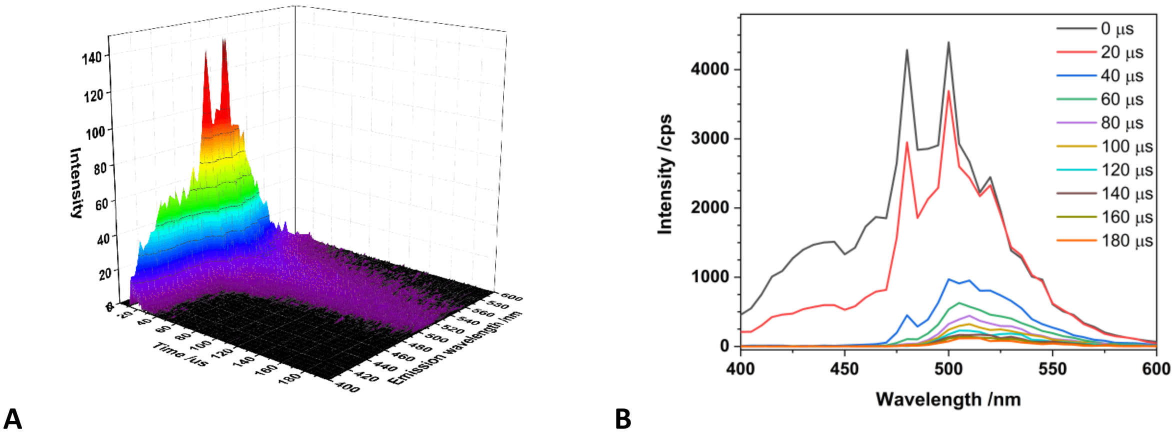

Figure 1.8 Time resolved emission spectra map (A) and spectra recorded with increasing time delay (B) of **1-NO₃** in MeCN at room temperature. λ_{ex} = 287 nm.

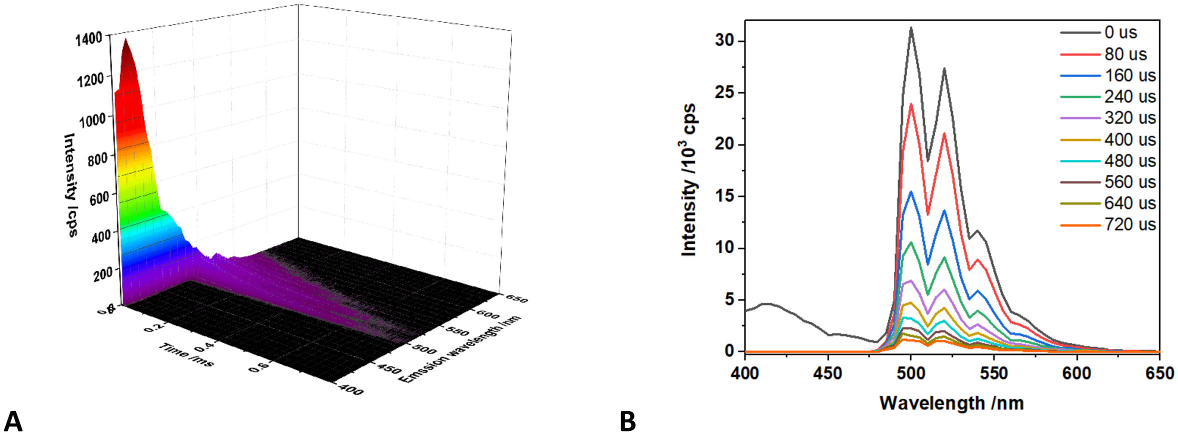

Figure 1.9 Low temperature (77 K) time resolved emission spectra map (A) and spectra recorded with increasing time delay sliced (B) of **1-NO$_3$** in frozen Me-THf. λ_{ex} = 320 nm.

Room temperature mission spectra of **1-Cl-MeCN** are very similar to those of **1-NO$_3$**, with two broad peaks centered at 450 and 520 nm, which can again be assigned to ph$_2$phen to uranium LMCT, and oxygen to uranium LMCT, respectively (Figure 1.10). Excitation of the complex at 427 and 440 nm, wavelengths of the lamps used for photocatalysis described in Chapter 2, leads to an identical emission peak centered at 520 nm, showing that the oxygen to uranium LMCT can be accessed at those irradiation wavelengths. The spectra obtained for the dimer **[1-Cl]$_2$** in acetonitrile are identical to those for **1-Cl-MeCN**, proving that the dimer dissociates to a monomer in MeCN solution. Room temperature lifetime of the uranyl LMCT emission centered at 521 nm for **1-Cl-MeCN** (16.19 (20%) and 69.67 (80%) µs) is higher than for **1-NO$_3$**.

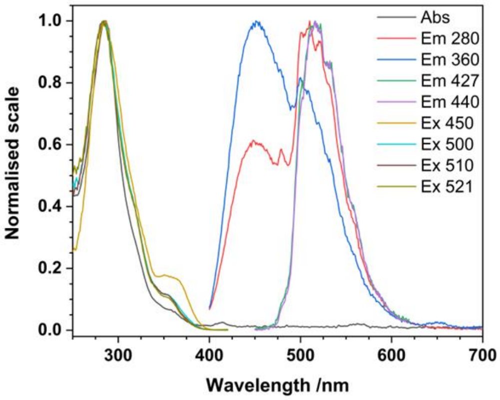

Figure 1.10 Absorption, emission, and excitation spectra of **1-Cl-MeCN** in acetonitrile at room temperature.

Binding of the second ph$_2$phen ligand to the uranyl(VI) center in **2** yields a significantly more intense oxo-to-uranium LMCT peak in the UV/vis spectrum. The molar absorption coefficient, ε, of this transition (λ_{max} 452) is 218 M^{-1} cm^{-1}, which is relatively high - the charge transfer is formally Laporte forbidden in a centrosymmetric complex and is usually below 10 M^{-1} cm^{-1}. However, deviation from centrosymmetric symmetry in uranyl complexes relaxes the Laporte rule,[1] hence the bending of the uranyl unit in **2** might explain the high ε value. In the room temperature emission spectrum (Figure 1.11, left), the uranyl LMCT emission centered at *ca.* 520 nm is clearly apparent alongside a higher energy broad feature at 381 nm, which is much shorter lived (μs <) than the uranyl LMCT emission (36 μs (25%), 120 μs (75%)), can be removed using a time gate, and is assigned to ph$_2$phen fluorescence. When cooled to liquid nitrogen temperature (Figure 1.11, right), the uranyl emission exhibits more well resolved vibrational progression due to reduced non-radiative vibrational decay; this is accompanied by the disappearance of ligand fluorescence indicating that the intra ligand π-π* excitations are involved in the energy migration pathway to afford uranyl LMCT emission and that that these energy transfer process, are more efficient at 77 K.[17] The excitation spectrum of the uranyl(VI) emission (centered at *ca.* 330 nm) is also different to the absorption spectrum and exhibits vibronic fine structure, again, suggesting that the equatorial ph$_2$phen to uranium LMCT excitation is responsible for the observed typical uranyl(VI) emission as observed with compound **1-NO$_3$**.

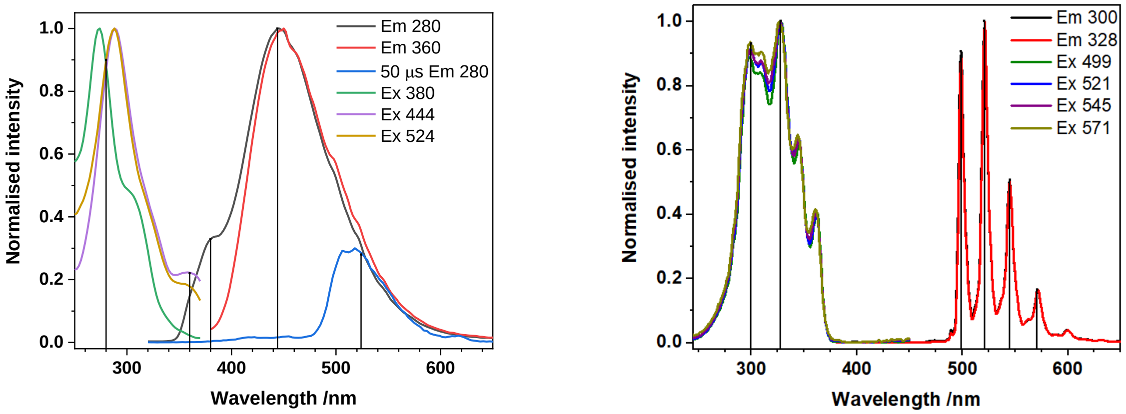

Figure 1.11 Left: absorption, emission, and excitation spectra of **2** in MeCN recorded at room temperature in fluid solution. Right: low temperature (77 K) emission and excitation spectra of **2** in frozen Me-THF.

Time resolved measurements of room temperature MeCN solutions of **2** (Figure 1.12) show that, similar to **1-NO$_3$**, the uranyl emission is much longer lived than the equatorial LMCT emission. In frozen solution at 77 K in Me-THF, the uranyl emission possesses a lifetime of ~303 μs (Figure 1.13).

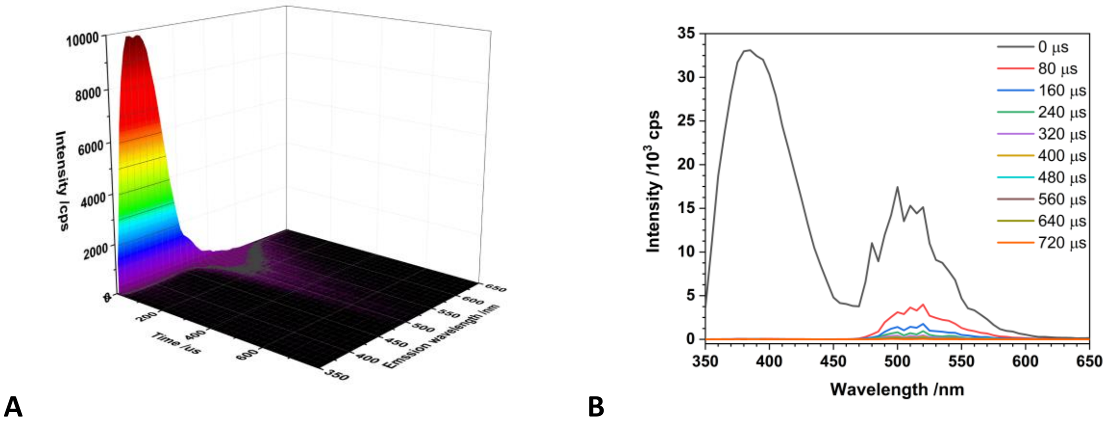

Figure 1.12 Time resolved emission spectra map (A) and time sliced spectra (B) of **2** in MeCN at room temperature. λ_{ex} = 274 nm.

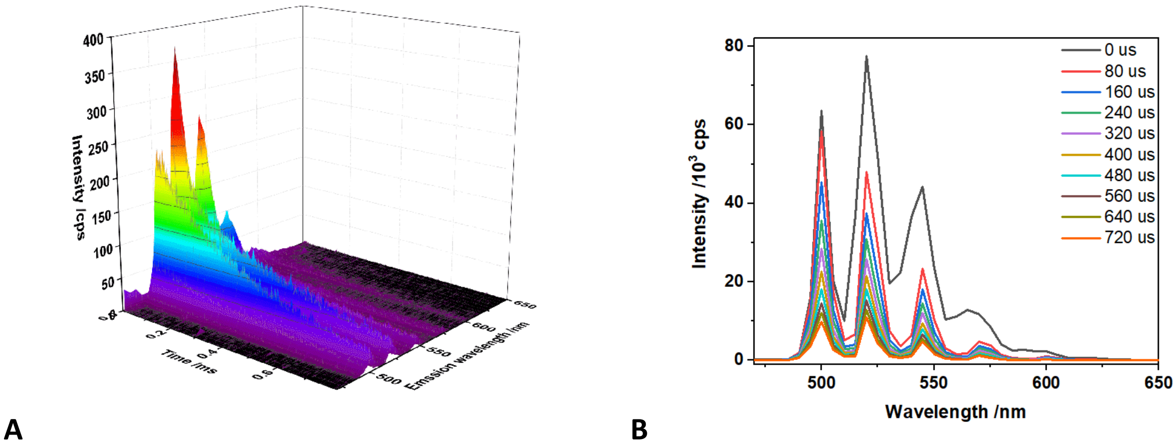

Figure 1.13 Low temperature (77 K) time resolved emission spectra map (A) and time sliced spectra (B) of **2** in frozen Me-THF, λ_{ex} = 328 nm.

The measured uranyl LMCT emission lifetimes of **1-Cl-MeCN** and **2** are significantly higher than in **1-NO$_3$**. Similarly, the emission lifetime of uranyl chloride acetonitrile solvate ([$UO_2Cl_2(MeCN)$]) in acetonitrile (93.7 µs) is longer than that of uranyl nitrate ([$UO_2(NO_3)_2 \cdot 6H_2O$]) (20.4 µs), also in acetonitrile. This could possibly be due to less vibrational quenching occurring with the chloride complexes or due to the chloride structures being less centrosymmetric.

1.3.3 Computational studies

To gain insight into the electronic structure of the aforementioned uranyl complexes, density-functional theory (DFT) calculations were performed using the PBE and PBE0 functional with a scalar relativistic ZORA Hamiltonian, and the small frozen core TZP basis set for all elements. Relevant molecular orbitals and their relative energies for **1-Cl-MeCN** in the ground state are shown in Figure 1.14. The unoccupied 5*f* orbitals on uranium (LUMO, LUMO+1, LUMO+2 and LUMO+3) are split into two levels due to the coordination field effect caused by chloride ions. The calculated HOMO is of a π type and is based on the ph_2phen ligand, whereas the σ_u MO, one originating from the covalent mixture of O-2*p* and U-5*f* orbitals, is much lower in energy. By comparison, the first few HOMO orbitals in uranyl nitrate are of a σ_u type (Figure 1.15).

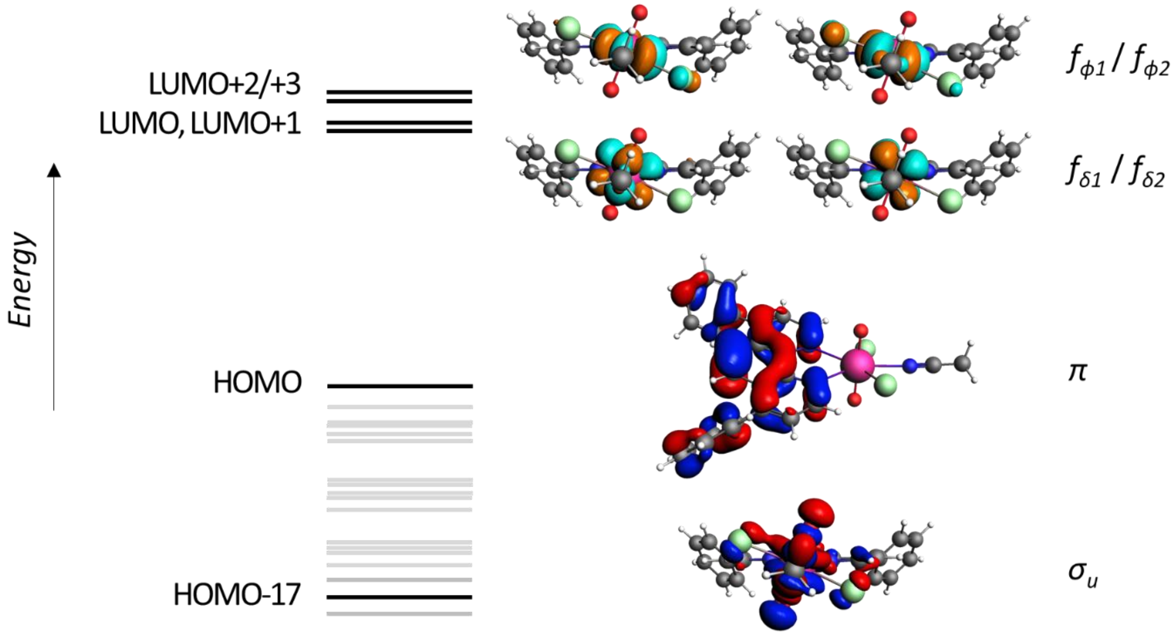

Figure 1.14 The orbital energy levels of **1-Cl-MeCN** calculated at the scalar−ZORA PBE0/TZP level of theory. Color code: pink – U, red – O, light green – Cl, blue – N, grey – C, white – H.

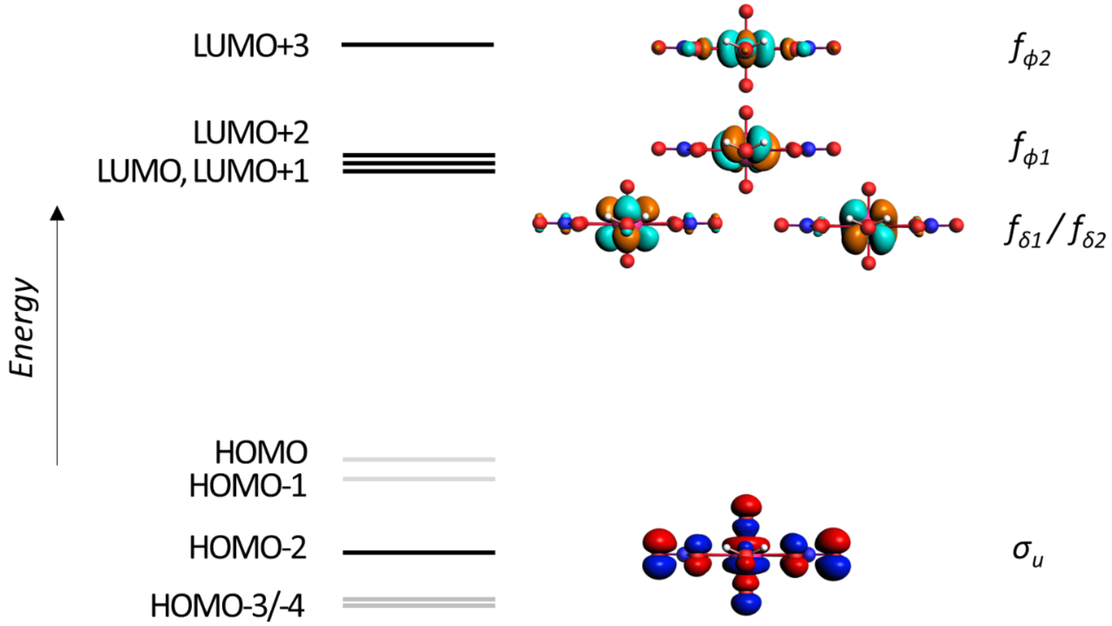

Figure 1.15 The orbital energy levels of $UO_2(NO_3)_2(H_2O)_2$ calculated at the scalar−ZORA PBE0/TZP level of theory. Color code: pink – U, red – O, blue – N, grey – C, white – H.

Calculations of spin densities of uranyl nitrate, uranyl chloride, **1-Cl-MeCN** and **2** in the lowest energy triplet (T_1) state show significant differences between the ph$_2$phen-ligated complexes and the other two compounds. While uranyl nitrate and uranyl chloride display oxyl radical character, both ph$_2$phen ligated complexes show radical delocalized over the ph$_2$phen ligand instead (Figure 1.15). In complex **2**, the spin is on the ph$_2$phen ligand that is oriented axially (parallel to the uranyl) rather than the ligand in the equatorial plane. The differences between these complexes are further seen in the singly occupied orbitals that arise from the first four vertical excitations in **1-Cl-MeCN** (Table 1.1) compared to uranyl nitrate (Table 1.2). While the higher energy singly occupied molecular orbitals (SOMOs) are of *f* character in both cases, the lower energy SOMO in **1-Cl-MeCN** is based on the π system in the ph$_2$phen ligand, instead of showing oxyl radical character. In contrast, the σ_u SOMOs clearly show oxyl radical character in uranyl nitrate. The consequences of these differences on the photocatalytic reactivity of **1-Cl-MeCN** are discussed in Chapter 2.

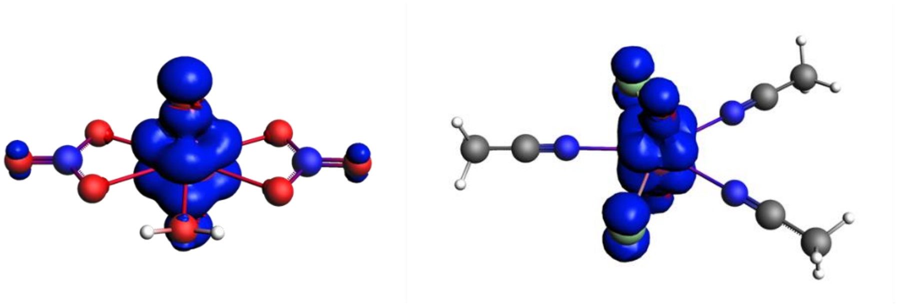

$UO_2(NO_3)_2(H_2O)_2$ $UO_2Cl_2(MeCN)_3$

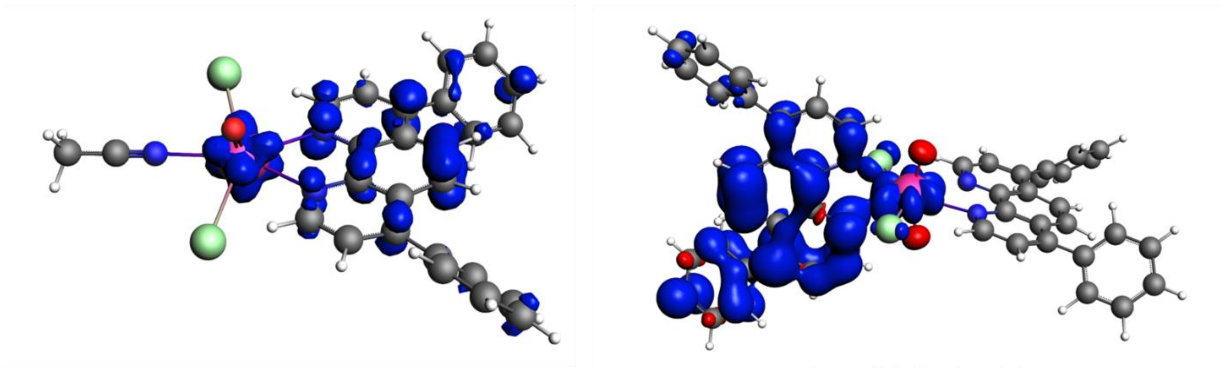

1-Cl-MeCN ($UO_2Cl_2(ph_2phen)(MeCN)$) **2** ($UO_2Cl_2(ph_2phen)_2$)

Figure 1.15 T_1 state spin density of [$UO_2(NO_3)_2(H_2O)_2$] (top-left), [$UO_2Cl_2(MeCN)_3$] (top-right), **1-Cl-MeCN** (bottom-left) and **2** (bottom-right) calculated at the scalar−ZORA PBE0/TZP level of theory, shown in blue. Color code: pink – U, red – O, light green – Cl, blue – N, grey – C, white - H.

Table 1.1 Vertical excitation energies (ΔE, kcal/mol), natural transition orbitals and the character of the singly occupied orbitals for different transitions of **1-Cl-MeCN** calculated at the scalar−ZORA TD-DFT PBE0/TZP level of theory. Color code: pink – U, red – O, light green – Cl, blue – N, grey – C, white – H.

Transitions	***ΔE***	**Singly occupied orbitals**	
#1 $S_0 \rightarrow {}^1(\pi f_{\phi 1})$	74	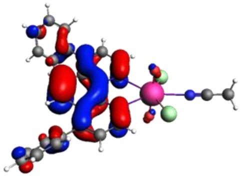 π	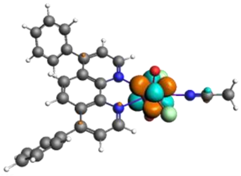 $f_{\delta 1}$
#2 $S_0 \rightarrow {}^1(\pi f_{\delta 1})$	74	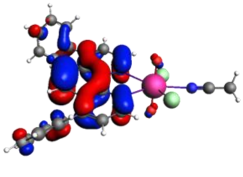 π	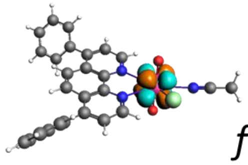 $f_{\delta 2}$
#3 $S_0 \rightarrow {}^1(\pi f_{\delta 2})$	76	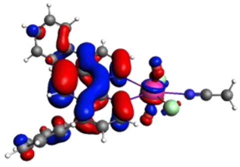 π	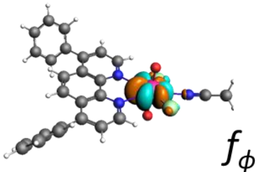 $f_{\phi 1}$
#4 $S_0 \rightarrow {}^1(\pi f_{\phi 2})$	77	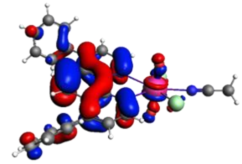 π	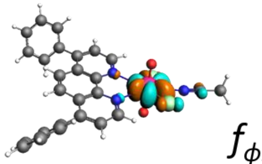 $f_{\phi 2}$

Table 1.2 Vertical excitation energies (ΔE, kcal/mol), natural transition orbitals and the character of the singly occupied orbitals for different transitions of [$UO_2(NO_3)_2(H_2O)_2$] calculated at the scalar−ZORA TD-DFT PBE0/TZP level of theory. Color code: pink – U, red – O, blue – N, grey – C, white – H.

Transitions	***ΔE***	**Singly occupied orbitals**	
#1 $S_0 \rightarrow {}^1(\sigma_u f_{\phi 1})$	86	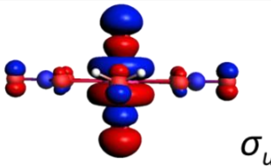 σ_u	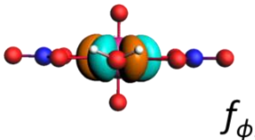 $f_{\phi 1}$
#2 $S_0 \rightarrow {}^1(\sigma_u f_{\delta 1})$	95	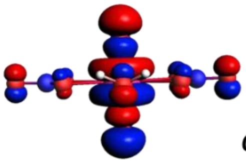 σ_u	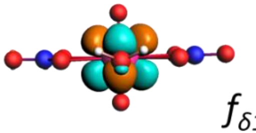 $f_{\delta 1}$
#3 $S_0 \rightarrow {}^1(\sigma_u f_{\delta 2})$	95	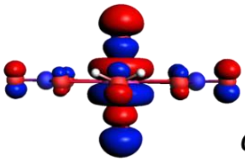 σ_u	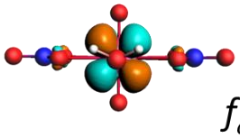 $f_{\delta 2}$
#4 $S_0 \rightarrow {}^1(\sigma_u f_{\phi 2})$	98	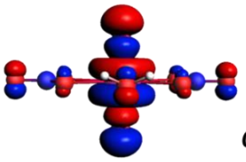 σ_u	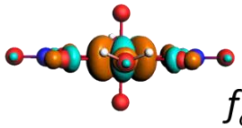 $f_{\phi 2}$

1.4 Conclusions

This chapter presents the syntheses of a new family of uranyl chloride ph$_2$phen complexes. With one equivalent of the ph$_2$phen ligand, a monomeric and a dimeric complex can be isolated depending on the solvent. While the structures of the *mono* ph$_2$phen complexes are unremarkable, the *bis* ph$_2$phen complex displays a significantly bent uranyl unit in the solid state. Luminescence spectra of ph$_2$phen-ligated complexes show two emission peaks: the ph$_2$phen ligand to uranium charge transfer at higher energy and the longer-lived oxygen to uranium LMCT at lower energy. The luminescence lifetimes of uranyl chloride complexes were found to be significantly longer than those for uranyl nitrate species, for example 16.19 (20%) and 69.67 (80%) µs for **1-Cl-MeCN** *vs*. 4.68 (20%) and 13.9 µs (80%) for **1-NO$_3$**. DFT calculations show that the ph$_2$phen complexes in the triplet excited state contain an unpaired electron in the π system of the ph$_2$phen ligand instead of showing oxyl radical character.

1.5 Experimental details

Solvents and reagents. Bathophenanthroline (ph_2phen) was purchased from Sigma Aldrich and purified before use by dissolving it in methanol, running the solution through a silica plug, and removing volatiles in *vacuo*. The solid was then recrystallized from hot toluene. Other chemicals and solvents were purchased from Sigma Aldrich or Fisher Scientific and used without purification. Deuterated solvents were purchased from Cambridge Isotope Laboratories.

Characterization. NMR spectra were recorded on Bruker Avance 400 MHz spectrometers and referenced to solvent residual signals (^{1}H, ^{13}C).[19] Chemical shifts are quoted in ppm and coupling constants in Hz. NMR spectra were taken at 25°C. UV/vis spectra were recorded with a Varian Cary 50 spectrophotometer. ATR-IR spectra were recorded using a Thermo Scientific Nicolet iS10 FTIR or a Shimadzu IRSpirit FTIR spectrometer. Absorption bands are reported in wavenumbers (cm^{-1}) with a note on intensity: s – strong; m – medium; w – weak. Elemental analyses were carried out by Dr. Elena Kreimer at the microanalytic facility in the College of Chemistry at the University of California, Berkeley with a Perkin Elmer CHNS 2400 Series II analyzer.

Crystallography. Single crystal X-ray diffraction data were collected using a Rigaku Xtalab Synergy-S diffractometer fitted with a HyPix-6000HE photon counting detector using MoKα ($\lambda = 0.71073$ Å) radiation. All structures were solved using SHELXT in Olex2 and refined using SHELXL in Olex2.[20,21] Absorption corrections were completed using CrysAlis PRO (Rigaku Oxford Diffraction) software. Analytical numeric absorption corrections used a multifaceted crystal model based on expressions derived by Clark and Reid.[22] Numerical absorption correction was based on a Gaussian integration over a multifaceted crystal model. All non-hydrogen atoms were refined with anisotropic displacement parameters and H-parameters were constrained to parent atoms and refined using a riding model.

Luminescence measurements. Luminescence measurements were recorded for solutions prepared in spectroscopic grade solvents made to an optical density of *ca.* 0.1 at the wavelength of excitation (*ca.* 10^{-5} M). Steady state emission and excitation spectra were recorded on an Edinburgh Instruments FP920 Phosphorescence Lifetime Spectrometer equipped with a 450 W steady state xenon lamp, a 5 W microsecond pulsed xenon flashlamp, with single 300 mm focal length excitation and emission monochromators in Czerny Turner configuration, and a red sensitive photomultiplier in Peltier (air cooled) housing (Hamamatsu R928P). Low temperature measurements were obtained using a sample in 2-methyl tetrahydrofuran (MeTHF) contained in NMR tubes, flash frozen with liquid nitrogen (77 K) and suspended in a finger Dewar with a quartz window. Lifetime data were recorded following excitation with the microsecond flashlamp using multichannel scanning (PCS900 plug-in PC card for fast photon counting). Lifetimes were obtained by tail fit on the data obtained and quality of fit judged by minimization of reduced χ-squared and residuals squared. The estimated error for lifetime measurements is +/- 10%.

Computational details. Unless specified, all calculations were carried out using the ADF 2021 software package,[23,24] the PBE[25] and PBE0[26,27] functional with a scalar relativistic ZORA Hamiltonian,[28–30] and the small frozen core TZP basis set for all elements.[31] All geometry optimizations were carried out in conjunction with the COSMO[32] implicit solvation model. The radii values of the atomic spheres in the COSMO solvation model for atoms in this study are the corresponding van der Waals radii from the MM3 method by Allinger[33] divided by 1.2. We note that the heavy uranium metal is well buried inside of the first solvation shell and does not have direct contact with the solvation cavity. Hence, its radius setting does not affect the results of the geometry optimization. The spin-orbit coupling effect was not considered in this work as, for the types of compounds studied here, it has only a minor effect on molecular structures, vibrational frequencies, and reaction energies. Grimme's D3 dispersion[34] correction with Becke-Johnson damping (D3BJ)[35] was used for the actinyl systems. Frequency calculations were performed to ensure optimization convergence to local minima and transition states on the potential energy surface. Scalar relativistic effects were included with the ZORA Hamiltonian and the corresponding basis set ZORA-def2-TZVP. [36]

Synthesis of UO_2Cl_2(MeCN). Uranyl chloride hydrate ($UO_2Cl_2·3H_2O$) was stirred in dry MeCN for 1 hr. The solvent was then removed *in vacuo* and the resulting yellow solid was further dried *in vacuo* for 5 hrs. The solid is sparingly soluble in MeCN and pyridine, and is not soluble in chloroform, DCM, chlorobenzene, and *ortho*-difluorobenzene. Crystals of the complex were grown from a concentrated MeCN solution at –30°C in an N_2 atmosphere glovebox, but desolvated immediately when put on a microscope slide. The NMR of the solid in DMSO with a methyl acetate internal standard shows 1 equivalent of MeCN coordinated to uranyl chloride.

^{1}H NMR (400 MHz, DMSO-d_6): δ 2.04 (CH_3CN). **UV/vis** (MeCN), λ_{max}/nm: 244, 433. The ε values could not be calculated due to low solubility of the complex in acetonitrile. **IR** (cm^{-1}): 2308 (w), 2280 (w), 1357 (w), 953 (s). **Elemental analysis**: expected C, 6.29%, H, 0.79%, N, 3.67%; found C, 6.70%, H, 0.86%, N, 3.85%.

Synthesis of UO_2Cl_2(ph_2phen)(MeCN) (1-Cl-MeCN). The slow addition of an acetonitrile suspension of 1 equivalent of ph_2phen to a stirred acetonitrile solution of a uranyl chloride hydrate ($UO_2Cl_2·3H_2O$) in acetonitrile results in a color change from yellow to light orange. A small amount of fluorescent yellow precipitate (the *bis*-ph_2phen complex **2**) forms as well. The subsequent removal of solvent *in vacuo* yields an orange solid that is soluble in acetonitrile and acetone. Attempts to crystallize the complex from MeCN were unsuccessful, however, the THF solvate **UO_2Cl_2(ph_2phen)(THF) (1-Cl-THF)** was crystallized by vapor diffusion of hexanes to a THF solution of crude **1-Cl-MeCN**.

^{1}H NMR (400 MHz, CD_3CN): δ 11.26 (s, 2H, N=CH_{phen}), 8.18 (s, 4H, CH_{phen}), 7.65 (d, *J* = 5.5 Hz, 10H, CH_{ph}). **UV/vis** (MeCN), λ_{max}/nm (ε/M^{-1} cm^{-1}): 421-484 (56 at 452 nm). **IR** (cm^{-1}): 1589 (w), 1522 (w), 925 (s), 834 (m), 764 (s), 734 (m), 701 (s), 630 (m), 574 (m), 545 (w).

Synthesis of [UO_2Cl_2(ph_2phen]$_2$ ([1-Cl]$_2$). Crystals of the dimer **[1-Cl]$_2$** were grown by vapor diffusion of hexanes to a chlorobenzene solution of crude **1-Cl-MeCN**.

The NMR spectrum of **[1-Cl]$_2$** in CD_3CN is identical to that of **1-Cl-MeCN**. **IR** (cm^{-1}): 1591 (w), 1555 (w), 1522 (w), 1092 (w), 935 (s), 835 (m), 764 (m), 735 (m), 701 (s), 630 (m), 575 (m), 545 (w). **UV/vis** (DCM), λ_{max}/nm: 422-486. **Elemental analysis**: expected C, 42.81%, H, 2.40%, N, 4.16%; found C, 42.47%, H, 2.60%, N, 3.81%.

Synthesis of $UO_2Cl_2(ph_2phen)_2$ (2). The addition of an acetonitrile suspension of $UO_2Cl_2 \cdot 3H_2O$ (440.2 mg; 1.128 mmol) to a stirred suspension of 2 equivalents of ph_2phen (750.0 mg; 2.256 mmol), also in acetonitrile, immediately resulted in the precipitation of a fluorescent yellow powder. The solid was then washed sequentially with acetonitrile and diethyl ether, and dried *in vacuo* to yield $[UO_2Cl_2(ph_2phen)_2]$ (1.0122 g; 89% yield). The solid is not soluble in acetonitrile or acetone but is sparingly soluble in chloroform and DCM. Single crystals suitable for SC-XRD were grown by layering a DCM solution of the complex with hexanes.

^{1}H NMR (400 MHz, CD_3Cl): δ 10.14 (d, *J* = 5.2 Hz, 2H, $N{=}CH_{phen}$), 8.21 (s, 2H, CH_{phen}), 7.90 (d, *J* = 5.2 Hz, 2H, CH_{phen}) and 7.61 (m, 10H, CH_{ph}). **UV/vis** (MeCN), λ_{max}/nm (ε/M^{-1} cm^{-1}): 452 (218), 282 (43600). **IR** (cm^{-1}): 1560 (m), 1427 (m), 900 (s), 855 (m), 832 (m), 774 (m), 741 (m), 700 (s), 628 (m), 575 (m), 545 (m). **Elemental analysis**: expected C, 57.32%, H, 3.21%, N, 5.57%; found C, 56.09%, H, 3.07%, N, 5.34%.

Table 1.3 Crystal data and structure refinement for **1-Cl-THF** and **[1-Cl]₂**.

Complex	**1-Cl-THF**	**[1-Cl]$_2$**
Empirical formula	$C_{28}H_{24}Cl_2N_2O_3U$	$C_{60}H_{42}Cl_6N_4O_4U_2$
Formula weight	745.42	1571.73
Temperature/K	100.00(10)	99.98(12)
Crystal system	monoclinic	monoclinic
Space group	*P*2$_1$/*n*	*C*2/*c*
a/Å	9.06020(10)	14.4589(2)
b/Å	18.1719(2)	26.3459(4)
c/Å	15.7262(2)	14.4152(2)
α/°	90	90
β/°	97.1350(10)	89.3990(10)
γ/°	90	90
Volume/Å^3	2569.13(5)	5490.92(14)
Z	4	4
ρ_{calc}g/cm^3	1.927	1.901
μ/mm^{-1}	6.559	6.235
F(000)	1424.0	2992.0
Crystal size/mm^3	0.27 × 0.22 × 0.08	0.372 × 0.087 × 0.042
Radiation	Mo Kα (λ = 0.71073)	Mo Kα (λ = 0.71073)
2Θ range for data collection/°	3.44 to 54.968	4.188 to 55.754
Index ranges	-11 ≤ h ≤ 11, -23 ≤ k ≤ 23, -20 ≤ l ≤ 20	-18 ≤ h ≤ 19, -34 ≤ k ≤ 34, -18 ≤ l ≤ 18
Reflections collected	109761	115436
Independent reflections	5903 [R_{int} = 0.0525, R_{sigma} = 0.0178]	6560 [R_{int} = 0.0639, R_{sigma} = 0.0230]
Data/restraints/parameters	5903/0/325	6560/355/407
Goodness-of-fit on F^2	1.033	1.063
Final R indexes [I>=2σ (I)]	R_1 = 0.0167, wR_2 = 0.0363	R_1 = 0.0261, wR_2 = 0.0547
Final R indexes [all data]	R_1 = 0.0202, wR_2 = 0.0371	R_1 = 0.0426, wR_2 = 0.0623
Largest diff. peak/hole / e Å^{-3}	1.08/-0.60	2.21/-0.95

Table 1.4 Crystal data and structure refinement for **2**.

Complex	**2**
Empirical formula	$C_{48}H_{32}Cl_2N_4O_2U$
Formula weight	1005.70
Temperature/K	99.99(13)
Crystal system	orthorhombic
Space group	$P2_12_12_1$
a/Å	12.2797(2)
b/Å	12.7824(2)
c/Å	24.6681(3)
α/°	90
β/°	90
γ/°	90
Volume/Å^3	3872.00(10)
Z	4
ρ_{calc}g/cm^3	1.725
μ/mm^{-1}	4.377
F(000)	1960.0
Crystal size/mm^3	0.201 × 0.058 × 0.025
Radiation	Mo Kα (λ = 0.71073)
2Θ range for data collection/°	3.588 to 62.054
Index ranges	$-17 \le h \le 17$, $-17 \le k \le 16$, $-35 \le l \le 35$
Reflections collected	90543
Independent reflections	10857 [R_{int} = 0.0600, R_{sigma} = 0.0402]
Data/restraints/parameters	10857/0/514
Goodness-of-fit on F^2	1.021
Final R indexes [I>=2σ (I)]	R_1 = 0.0246, wR_2 = 0.0430
Final R indexes [all data]	R_1 = 0.0316, wR_2 = 0.0443
Largest diff. peak/hole / e Å^{-3}	1.09/-0.71
Flack parameter	-0.012(2)

1.6 References

(1) Natrajan, L. S. Developments in the Photophysics and Photochemistry of Actinide Ions and Their Coordination Compounds. *Coord Chem Rev* **2012**, *256* (15–16), 1583–1603. https://doi.org/10.1016/j.ccr.2012.03.029.

(2) Wang, W.-D.; Bakac, A.; Espenson, J. H. *Uranium(VI)-Catalyzed Photooxidation of Hydrocarbons with Molecular Oxygen*; 1995; Vol. 34. https://pubs.acs.org/sharingguidelines.

(3) Yu, Z. J.; Chen, H.; Lennox, A. J. J.; Yan, L. J.; Liu, X. F.; Xu, D. D.; Chen, F.; Xu, L. X.; Li, Y.; Wu, Q. A.; Luo, S. P. Heteroleptic Copper(I) Photosensitizers with Carbazole-Substituted Phenanthroline Ligands: Synthesis, Photophysical Properties and Application to Photocatalytic H2 Generation. *Dyes and Pigments* **2019**, *162*, 771–775. https://doi.org/10.1016/j.dyepig.2018.10.067.

(4) Xu, L. X.; Wang, T. Q.; Liu, X. F.; Chen, H.; Wei, C. J.; Xu, D. D.; Chen, F.; Li, Y.; Luo, S. P. The Heteroleptic Cu(I) Photosensitizer-Containing 3,8-Disubstituted Phenanthroline: Synthesis, Photophysical Properties and Photocatalytic Hydrogen Evolution from Water. *Eur J Inorg Chem* **2020**, *2020* (45), 4278–4283. https://doi.org/10.1002/ejic.202000648.

(5) Pirtsch, M.; Paria, S.; Matsuno, T.; Isobe, H.; Reiser, O. [Cu(Dap)2Cl] As an Efficient Visible-Light-Driven Photoredox Catalyst in Carbon-Carbon Bond-Forming Reactions. *Chemistry - A European Journal* **2012**, *18* (24), 7336–7340. https://doi.org/10.1002/chem.201200967.

(6) Morozkov, G. V.; Abel, A. S.; Filatov, M. A.; Nefedov, S. E.; Roznyatovsky, V. A.; Cheprakov, A. V.; Mitrofanov, A. Y.; Ziankou, I. S.; Averin, A. D.; Beletskaya, I. P.; Michalak, J.; Bucher, C.; Bonneviot, L.; Bessmertnykh-Lemeune, A. Ruthenium(Ii) Complexes with Phosphonate-Substituted Phenanthroline Ligands: Synthesis, Characterization and Use in Organic Photocatalysis. *Dalton Transactions* **2022**, *51* (36), 13612–13630. https://doi.org/10.1039/d2dt01364a.

(7) Accorsi, G.; Listorti, A.; Yoosaf, K.; Armaroli, N. 1,10-Phenanthrolines: Versatile Building Blocks for Luminescent Molecules, Materials and Metal Complexes. *Chem Soc Rev* **2009**, *38* (6), 1690–1700. https://doi.org/10.1039/b806408n.

(8) Lu, H.; Zheng, Z.; Qiu, J.; Qian, Y.; Wang, J. Q.; Lin, J. Unveiling the New Function of Uranyl Molecular Clusters as Fluorometric Sensors for UV and X-Ray Dosimetry. *Dalton Transactions* **2022**, *51* (8), 3041–3045. https://doi.org/10.1039/d1dt04225d.

(9) McGlynn, S. P.; Smith, J. K.; Neely, W. C. Electronic Structure, Spectra, and Magnetic Properties of Oxycations. III. Ligation Effects on the Infrared Spectrum of the Uranyl Ion. *J Chem Phys* **1961**, *35* (1), 105–116. https://doi.org/10.1063/1.1731876.

(10) Ahuja, I. S.; Singh, R. 1,10-Phenanthroline Complexes of Some Uranyl Salts. *Journal of Inorganic and Nuclear Chemistry* **1973**, *35* (6), 2075–2078. https://doi.org/10.1016/0022-1902(73)80149-6.

(11) Schöne, S.; Radoske, T.; März, J.; Stumpf, T.; Patzschke, M.; Ikeda-Ohno, A. [UO $_2$ Cl $_2$ (Phen) $_2$], a Simple Uranium(VI) Compound with a Significantly Bent Uranyl Unit (Phen=1,10-

Phenanthroline). *Chemistry - A European Journal* **2017**, *23* (55), 13574–13578. https://doi.org/10.1002/chem.201703009.

(12) Arnold, P. L.; Purkis, J. M.; Rutkauskaite, R.; Kovacs, D.; Love, J. B.; Austin, J. Controlled Photocatalytic Hydrocarbon Oxidation by Uranyl Complexes. *ChemCatChem* **2019**, *11* (16), 3786–3790. https://doi.org/10.1002/cctc.201900037.

(13) Wilkerson, M. P.; Burns, C. J.; Paine, R. T.; Scott, B. L. Synthesis and Crystal Structure of UO2Cl2(THF)3: A Simple Preparation of an Anhydrous Uranyl Reagent. *Inorg Chem* **1999**, *38* (18), 4156–4158. https://doi.org/10.1021/ic990159g.

(14) Alcock, N. W.; Flanders, D. J.; Pennington, M.; Brown, D. Actinide Structural Studies. 15. Two 1,10-Phenanthroline Complexes of Uranium(VI). *Acta Crystallographica Section C* **1988**, *44* (2), 247–250. https://doi.org/10.1107/S010827018701103X.

(15) Alcock, N. W.; Flanders, D. J.; Brown, D. Actinide Structural Studies. Part 7. The Crystal and Molecular Structures of (2,2’-Bipyridyl)Dinitratodioxo-Uranium(vi) and -Neptunium(vi), and Diacetato-(2,2’-Bi Pyridyl)Dioxo-Uranium(vi) and -Neptunium (Vi). *Journal of the Chemical Society, Dalton Transactions* **1985**, No. 5, 1001–1007.

(16) Charpin, P.; Lance, M.; Nierlich, M.; Vigner, D.; Baudin, C. A Dimer of Dichlorodioxobis(Tetrahydrofuran)Uranium(VI). *Acta Crystallographica Section C* **1987**, *43* (9), 1832–1833. https://doi.org/10.1107/S0108270187089984.

(17) Redmond, M. P.; Cornet, S. M.; Woodall, S. D.; Whittaker, D.; Collison, D.; Helliwell, M.; Natrajan, L. S. Probing the Local Coordination Environment and Nuclearity of Uranyl(vi) Complexes in Non-Aqueous Media by Emission Spectroscopy. *Dalton Trans.* **2011**, *40* (15), 3914–3926. https://doi.org/10.1039/C0DT01464H.

(18) Lopez-Odriozola, L.; Walker, L.; Natrajan, L. S. General Properties and Reactions of The Actinides. *Reference Module in Chemistry, Molecular Sciences and Chemical Engineering, Elsevier* **2022**.

(19) Fulmer, G. R.; Miller, A. J. M.; Sherden, N. H.; Gottlieb, H. E.; Nudelman, A.; Stoltz, B. M.; Bercaw, J. E.; Goldberg, K. I. NMR Chemical Shifts of Trace Impurities: Common Laboratory Solvents, Organics, and Gases in Deuterated Solvents Relevant to the Organometallic Chemist. *Organometallics* **2010**, *29* (9), 2176–2179. https://doi.org/10.1021/om100106e.

(20) Dolomanov, O. V; Bourhis, L. J.; Gildea, R. J.; Howard, J. A. K.; Puschmann, H. OLEX2: A Complete Structure Solution, Refinement and Analysis Program. *J Appl Crystallogr* **2009**, *42* (2), 339–341. https://doi.org/10.1107/S0021889808042726.

(21) Sheldrick, G. M. SHELXT – Integrated Space-Group and Crystal-Structure Determination. *Acta Crystallographica Section A* **2015**, *71* (1), 3–8. https://doi.org/10.1107/S2053273314026370.

(22) Clark, R. C.; Reid, J. S. The Analytical Calculation of Absorption in Multifaceted Crystals. *Acta Crystallographica Section A* **1995**, *51* (6), 887–897. https://doi.org/10.1107/S0108767395007367.

(23) te Velde, G.; Bickelhaupt, F. M.; Baerends, E. J.; Fonseca Guerra, C.; van Gisbergen, S. J. A.; Snijders, J. G.; Ziegler, T. Chemistry with ADF. *J Comput Chem* **2001**, *22* (9), 931–967. https://doi.org/10.1002/jcc.1056.

(24) ADF . SCM, Theoretical Chemistry, Vrije Universiteit, Amsterdam, The Netherlands. . http://www.scm.com/. (accessed 2023-07-28).

(25) Perdew, J. P.; Burke, K.; Ernzerhof, M. *Generalized Gradient Approximation Made Simple*; 1996.

(26) Perdew, J. P.; Ernzerhof, M.; Burke, K. Rationale for Mixing Exact Exchange with Density Functional Approximations. *Journal of Chemical Physics* **1996**, *105* (22), 9982–9985. https://doi.org/10.1063/1.472933.

(27) Adamo, C.; Barone, V. Toward Reliable Density Functional Methods without Adjustable Parameters: The PBE0 Model. *Journal of Chemical Physics* **1999**, *110* (13), 6158–6170. https://doi.org/10.1063/1.478522.

(28) Van Lenthe, E.; Baerends, E. J.; Snijders, J. G. Relativistic Regular Two-Component Hamiltonians. *J Chem Phys* **1993**, *99* (6), 4597–4610. https://doi.org/10.1063/1.466059.

(29) Van Lenthe, E.; Baerends, E. J.; Snijders, J. G. Relativistic Total Energy Using Regular Approximations. *J Chem Phys* **1994**, *101* (11), 9783–9792. https://doi.org/10.1063/1.467943.

(30) Van Lenthe, E. Geometry Optimizations in the Zero Order Regular Approximation for Relativistic Effects. *Journal of Chemical Physics* **1999**, *110* (18), 8943–8953. https://doi.org/10.1063/1.478813.

(31) Van Lenthe, E.; Baerends, E. J. Optimized Slater-Type Basis Sets for the Elements 1-118. *J Comput Chem* **2003**, *24* (9), 1142–1156. https://doi.org/10.1002/jcc.10255.

(32) Pye, C.; Ziegler, T.; Lenthe, E.; Louwen, J. An Implementation of the Conductor-like Screening Model of Solvation within the Amsterdam Density Functional Package — Part II. COSMO for Real Solvents1. *Can J Chem* **2009**, *87*, 790–797. https://doi.org/10.1139/V09-008.

(33) Allinger, N. L.; Zhou, X.-Z.; Bergsma, J. S. Molecular Mechanics Parameters. *Journal of Molecular Structure-theochem* **1994**, *312*, 69–83.

(34) Grimme, S.; Antony, J.; Ehrlich, S.; Krieg, H. A Consistent and Accurate Ab Initio Parametrization of Density Functional Dispersion Correction (DFT-D) for the 94 Elements H-Pu. *Journal of Chemical Physics* **2010**, *132* (15). https://doi.org/10.1063/1.3382344.

(35) Grimme, S.; Ehrlich, S.; Goerigk, L. Effect of the Damping Function in Dispersion Corrected Density Functional Theory. *J Comput Chem* **2011**, *32* (7), 1456–1465. https://doi.org/10.1002/jcc.21759.

(36) Weigend, F.; Ahlrichs, R. Balanced Basis Sets of Split Valence, Triple Zeta Valence and Quadruple Zeta Valence Quality for H to Rn: Design and Assessment of Accuracy. *Physical Chemistry Chemical Physics* **2005**, *7* (18), 3297–3305. https://doi.org/10.1039/b508541a.

Chapter 2

Photocatalytic C-H bond functionalization by phenanthroline-based uranyl complexes

2.1 Overview

The photocatalytic reactivity of the complexes reported in Chapter 1 is tested for C-H bond fluorination, oxidation, and C-C bond coupling. DFT calculations are performed to compare the reaction activation barriers for the different catalysts. Finally, Stern-Volmer measurements are carried out with the cyclooctane substrate as well.

Stern-Volmer measurements discussed in this chapter were performed by Dr. Adam Woodward and Dr. Louise Natrajan at the University of Manchester and National Nuclear User Facility in the United Kingdom. Mechanistic calculations were done by Dr. Xiaobin Zhang and Prof. Georg Schreckenbach at the University of Manitoba, Canada. Single crystal XRD data for **[1-Cl-F]$_2$** was collected by Dr. Erik Ouellette and Sheridon Kelly at the Advanced Light Source (ALS) at Lawrence Berkeley National Lab. Support for the synthetic work was provided by the Office of Science, Office of Basic Energy Sciences, Division of Chemical Sciences, Geosciences, and Biosciences Heavy Elements Chemistry program of the U.S. Department of Energy under contract number DE-AC02-05CH11231 at LBNL.

2.2 Introduction

Functionalization of C(sp^3)-H bonds remains a long-lasting challenge in synthetic chemistry, as the dissociation energies of these bonds are relatively high (>80 kcal/mol and up to *ca*. 100 kcal/mol)[1]. Utilizing photocatalysis for this purpose has gained a lot of interest in recent years and a number of both organic and inorganic photocatalysts for hydrogen atom abstraction (HAA) have been developed, including complexes of the uranyl ion, UO_2^{2+}.[2]

Uranyl nitrate, $[UO_2(NO_3)_2(OH_2)_2]\cdot4H_2O$, has been shown to catalyze alkane fluorination by HAA and the subsequent quenching of the generated carbon-centered radical with an electrophilic fluorine source (Scheme 2.1).[3] Simple cyclic and linear saturated alkanes could be fluorinated in high yields (*e.g.* 95% for cyclooctane) under illumination by a high intensity lamp. Uranyl acetate, $[UO_2(OAc)_2\cdot4H_2O]$ was found to be an inferior photocatalyst to uranyl nitrate for the reaction. A computational investigation of the fluorination reaction found HAA from the cyclooctane substrate by the oxygen in the uranyl moiety to be the rate-limiting step.[4]

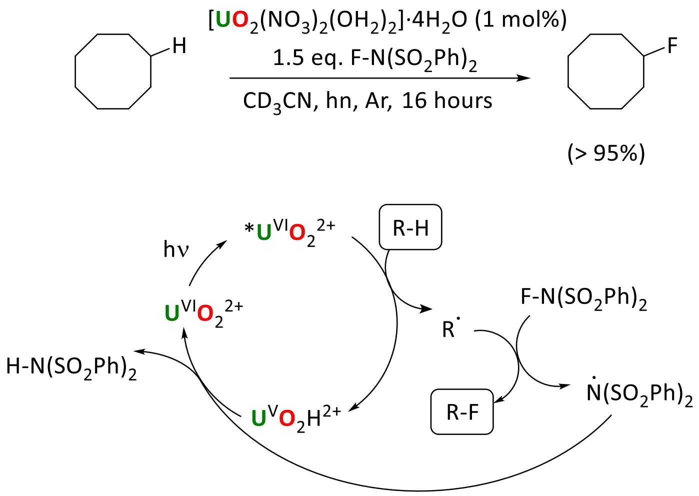

Scheme 2.1 Top: photocatalytic fluorination of unactivated sp^3 C-H bonds, here represented in the mono-fluorination of cyclooctane. Bottom: proposed mechanism of the catalytic cycle for the fluorination of alkanes.[3]

Uranyl nitrate has also been shown to be a catalyst for the addition of (cyclo)alkanes, ethers, acetals, and amides to electron-poor olefins.[5] Using uranyl acetate instead of uranyl nitrate was again detrimental to the reaction, with uranyl acetate not producing any detectable amount of product. Multiple uranyl complexes have been used to catalyze direct alkylation of *p*-quinone methides, feedstocks for diarylmethane derivatives with biological and pharmacological applications.[6] Uranyl acetate, uranyl sulfate [$UO_2SO_4 \cdot 4H_2O$], and uranyl triflate [$UO_2(OTf)_2 \cdot 6H_2O$] were all found to give lower yields than uranyl nitrate in these reactions. The differences in reactivity between the different uranyl complexes were not further investigated in all the cases mentioned above.

Uranyl chemistry is dominated by fast ligand exchange between the (normally) five ligands bound in the equatorial plane. To the best of the author's knowledge, in only three instances has a supporting (L-donor type) ligand been used to control uranyl coordination during photocatalytic HAA. A chiral uranyl salen complex, [UO_2(HOEt)(salen)] (salen=2,2′-((1E,1′E)-((1R,2R)-cyclohexane-1,2-diylbis(azanylylidene))bis(methanylylidene))diphenol), was used for α-cyanation of anilines (Scheme 2.2 A).[7] The phosphine oxide–solvated cation [$UO_2(OPCyPh_2)_4]^{2+}$ ($OPCyPh_2$ = cyclohexyldiphenylphosphine oxide) catalyzes the oxygenation by molecular O_2 of cyclohexene to four different oxygenated products *via* a uranyl(VI) peroxo intermediate (Scheme 2.2 B).[8] In 2019, our group reported the new uranyl-phenanthroline complex [$UO_2(NO_3)_2(ph_2phen)$] **1-NO₃** (ph_2phen = 4,7-diphenyl-1,10-phenanthroline) as a selective catalyst for the oxidation of benzylic C−H bonds as well as C−C bond cleavage in 2-phenoxy-1-phenylethanol (2P1PE), a model for the parts of lignin that are most challenging to cleave (Scheme 2.2 C).[9] We found that **1-NO₃** gives higher conversions than uranyl nitrate for all substrates tested.

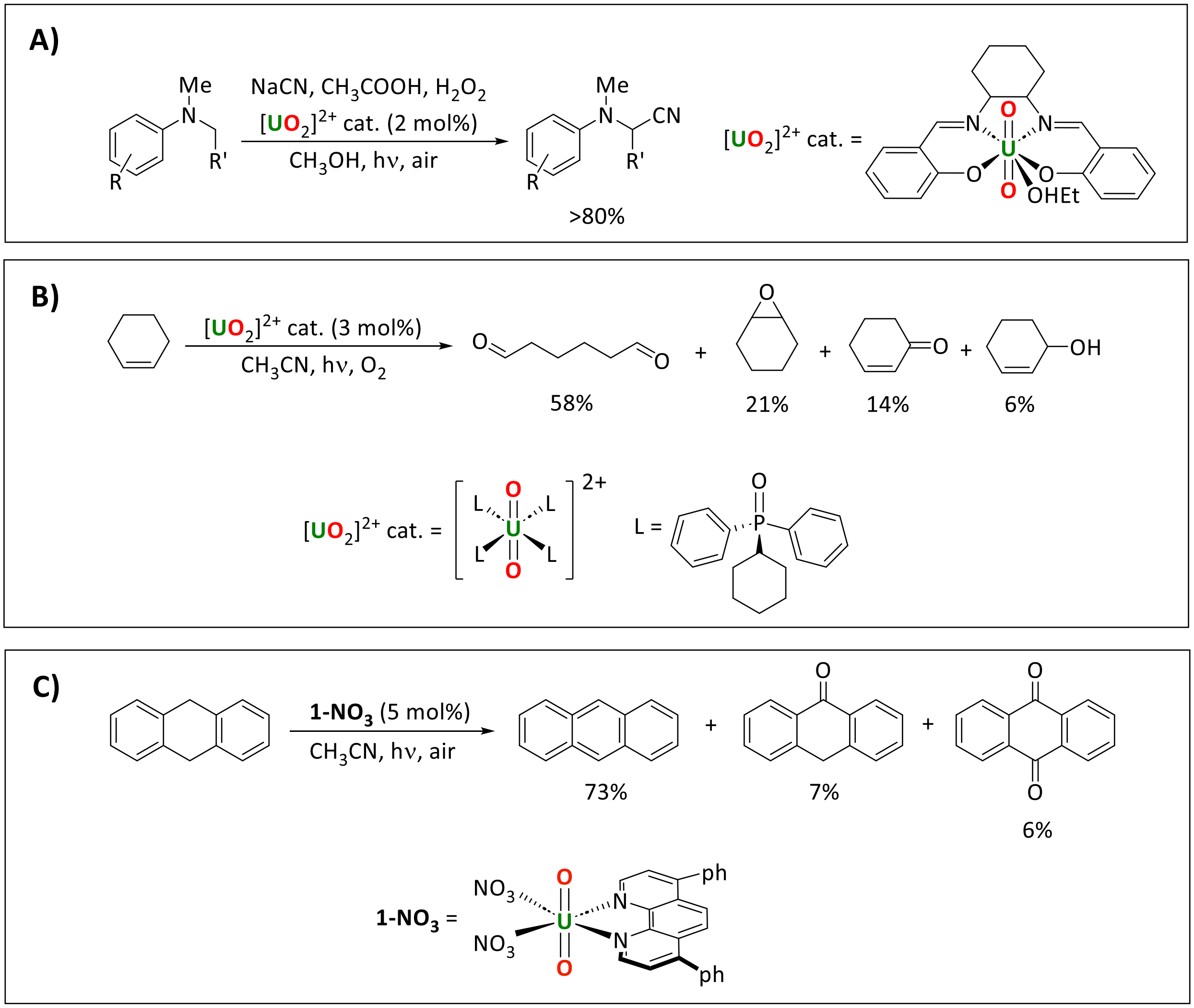

Scheme 2.2 Reported photocatalytic reactions that utilize uranyl complexes with L-type ligands. (A) [$UO_2(HOEt)(salen)$]; (B) [$UO_2(OPCyPh_2)_4$]$^{2+}$; (C) [$UO_2(NO_3)_2(ph_2phen)$] (**1-NO$_3$**).

Aside from hydrogen atom abstraction, the excited state of the uranyl ion ($*UO_2^{2+}$) can be quenched by organic molecules *via* multiple other pathways. $*UO_2^{2+}$ is a strong oxidant ($E^0 = +2.6$ V *vs*. SHE)[10] and can react with organic substrates through single electron transfer (SET). For example, uranyl acetate has recently been used for late-stage oxygenation of sulfur-containing molecules.[11] Aromatic compounds have also been shown to quench the excited state of uranyl through exciplex formation, both experimentally[12] and computationally.[4] This interaction leads to return of the excited uranyl ion to the ground state with no net chemical change in the reactants (Scheme 2.3).

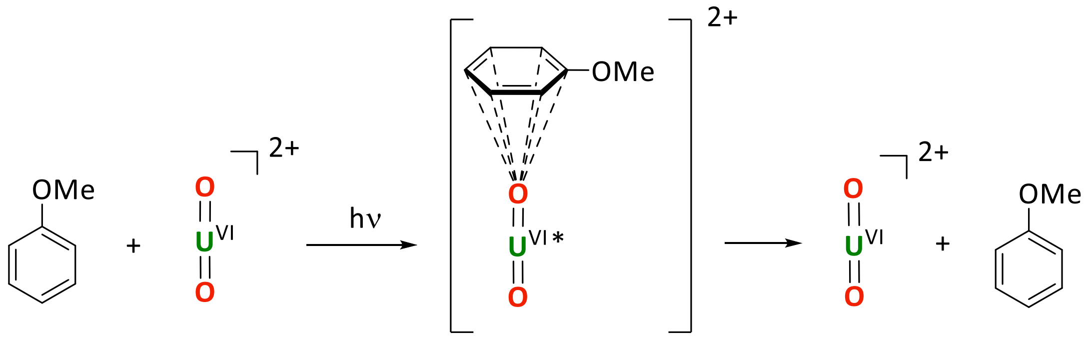

Scheme 2.3 Calculated physical quenching pathway for $*U^{VI}O_2^{2+}$ in the presence of aromatic substrates, here, exemplified with anisole. The scheme was adapted from Wu *et al*.[4]

2.3 Results and discussion

2.3.1 Fluorination reactions

The new uranyl chloride ph_2phen complexes reported in Chapter 1 were tested in photocatalytic fluorination reactions. Cyclooctane was chosen as a model substrate that contains a strong C-H bond (95.7 kcal/mol)[13] and yields fluorinated products easily tracked by proton and fluorine NMR. The reactions were carried out under anaerobic conditions in order to avoid an oxidation reaction that would lead to ketone and alcohol side products.[9] Acetonitrile was chosen as a solvent frequently used in uranyl photocatalysis. Similarly, *N*-fluorobenzenesulfonimide (NFSI), the fluorinating agent previously utilized by West *et al*. for alkane fluorination, was used.[3] LED lamps with specific emission wavelengths in the visible light region made by Kessil were used as light sources. Uranyl chloride acetonitrile adduct was selected as a water-free control reagent to gauge the effects of the ph_2phen ligand on the photocatalytic reactivity of the complexes. The reactions were all carried out overnight (16 h) and a summary of the reactions is shown in Scheme 2.4.

The amount of NFSI and reaction volume were both optimized. Increasing the amount of NFSI was found to improve fluorocyclooctane yields with $[UO_2Cl_2(MeCN)]$, but have essentially no effect when a ph_2phen-ligated complex was used (Table 2.1, entries 1-6). Even though 2 equivalents of NFSI gave the highest yield with $[UO_2Cl_2(MeCN)]$, 1.5 equiv. of NFSI was chosen for subsequent reactions as the option with better atom economy. Increasing the reaction volume was found to be detrimental to fluorocyclooctane yield with both **1-Cl-MeCN** (Table 2.1, entries 7 and 8) and **2** (Table 2.1, entries 5 and 9). Lower volumes could not be tested due to the limits of catalyst solubility in acetonitrile. Trace amounts (<1% yield) of cyclooctene were observed in a number of reactions, showing that cyclooctane dehydrogenation (*i.e.* abstraction of two H atoms) or dehydrohalogenation of fluorocyclooctane could also be achieved.

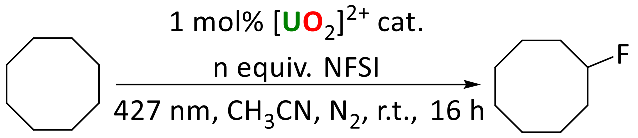

Scheme 2.4 Photocatalytic fluorination of cyclooctane. Optimization of NFSI amount and reaction volume.

Table 2.1 Cyclooctane fluorination reactions with varying NFSI loading and reaction volume.

Entry	[U] catalyst	NFSI equivalents	MeCN volume (mL)	Fluorocyclooctane yield (%)
1	$[UO_2Cl_2(MeCN)]$	1.0	1.0	8
2	$[UO_2Cl_2(MeCN)]$	1.5	1.0	26
3	$[UO_2Cl_2(MeCN)]$	2.0	1.0	33
4	$[UO_2Cl_2(ph_2phen)_2]$, **2**	1.0	1.0	43
5	$[UO_2Cl_2(ph_2phen)_2]$, **2**	1.5	1.0	40
6	$[UO_2Cl_2(ph_2phen)_2]$, **2**	2.0	1.0	41
7	$[UO_2Cl_2(ph_2phen)(MeCN)]$, **1-Cl-MeCN**	1.5	1.0	35
8	$[UO_2Cl_2(ph_2phen)(MeCN)]$, **1-Cl-MeCN**	1.5	10.0	32
9	$[UO_2Cl_2(ph_2phen)_2]$, **2**	1.5	10.0	29

Next, the catalyst loading and light source were optimized. 1 mol% was found to be the optimal catalyst loading as both higher and lower loadings of **2** gave lower fluorocyclooctane yields (Table 2.2, entries 1-3). The lower yield with 10 mol% of catalyst could possibly be due to the ph$_2$phen ligand quenching the excited state of the uranyl complex intermolecularly through exciplex decay as this effect would be increased at higher concentration of the catalyst. Since the uranyl complexes tested have broad absorptions in the 400-500 nm interval in their UV/vis spectra, multiple lamps that emit light in that range were tested. For complex **2**, fluorocyclooctane yields were almost identical when using 427, 440 and 467 nm light sources (Table 2.2, entries 2, 4, 5). Interestingly, for **1-Cl-MeCN** the use of a higher energy lamp (427 nm) gave the highest yield of fluorocyclooctane, while lower energy lamps produced more significant yields of the alkene side product (Table 2.2, entries 6-8). Higher catalyst loading of **1-Cl-MeCN** gave a lower fluorocyclooctane yield, possibly due to the ph$_2$phen ligand quenching the excited state of the catalyst; a small amount of the alkene product was again detected. Performing the fluorination reaction with one and two equivalents of ph$_2$phen ligand instead of a uranyl complex gave small yields of fluorocyclooctane. Finally, uranyl catalyst and light were both shown to be essential to the reaction.

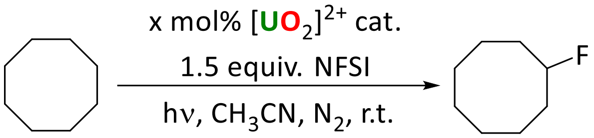

Scheme 2.5 Photocatalytic fluorination of cyclooctane. Optimization of catalyst loading and light source.

Table 2.2 Cyclooctane fluorination reactions with varying catalyst loading and light source.

Entry	[U] catalyst	Catalyst loading (mol%)	LED lamp wavelength, nm	Fluorocyclooctane yield (%)
1	[$UO_2Cl_2(ph_2phen)_2$], **2**	10	427	26
2	[$UO_2Cl_2(ph_2phen)_2$], **2**	1	427	40
3	[$UO_2Cl_2(ph_2phen)_2$], **2**	0.5	427	29
4	[$UO_2Cl_2(ph_2phen)_2$], **2**	1	440	39
5	[$UO_2Cl_2(ph_2phen)_2$], **2**	1	467	39
6	[$UO_2Cl_2(ph_2phen)(MeCN)$], **1-Cl-MeCN**	1	427	26
7	[$UO_2Cl_2(ph_2phen)(MeCN)$], **1-Cl-MeCN**	1	440	23; 4% yield of cyclooctene
8	[$UO_2Cl_2(ph_2phen)(MeCN)$], **1-Cl-MeCN**	1	467	25; 2% yield of cyclooctene
9	[$UO_2Cl_2(ph_2phen)(MeCN)$], **1-Cl-MeCN**	10	440	11; 3% yield of cyclooctene
10	none	0	440	trace
11	none (1 equiv. ph_2phen only)	0	440	8
12	none (2 equiv. ph_2phen only)	0	440	4
13	[$UO_2Cl_2(ph_2phen)(MeCN)$], **1-Cl-MeCN**	1	none	none

With the reaction conditions optimized, the reactivity of different uranyl photocatalysts was compared (Table 2.3). Both ph_2phen complexes showed improved yields of fluorocyclooctane compared to uranyl chloride acetonitrile adduct. However, uranyl nitrate, the photocatalyst previously used for alkane fluorination by West *et al.*,[3] was found to yield the highest amount of fluorocyclooctane.

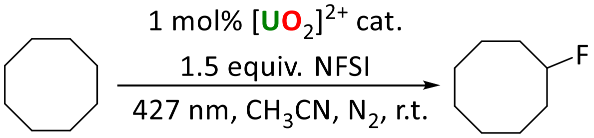

Scheme 2.6 Photocatalytic fluorination of cyclooctane using uranyl catalysts.

Table 2.3 Cyclooctane fluorination reactions with different uranyl photocatalysts.

[U] catalyst	Fluorocyclooctane yield (%)
[UO_2Cl_2(MeCN)]	26
[UO_2Cl_2(ph$_2$phen)(MeCN)], **1-Cl-MeCN**	35
[UO_2Cl_2(ph$_2$phen)$_2$], **2**	40
[$UO_2(NO_3)_2(OH_2)_2$]·$4H_2O$	46

Aside from **2**, all other uranyl catalysts were soluble in the reaction mixtures. However, even though **2** was not initially soluble, under the reaction conditions the complex dissolved fully within 1 minute of irradiation. The proton NMR spectrum of an aliquot taken after 5 and 10 minutes of the reaction shows the release of free ph$_2$phen as well as a small amount of another uranyl complex with a coordinated ph$_2$phen ligand. Storage of these aliquots in the dark overnight leads to precipitation of yellow crystals of the fluoride-bridged dimer **[1-Cl-F]$_2$** (Figure 2.1). The peak observed in the NMR spectra of the aliquots is hence assigned to this complex. This peak is not observed after 30 min of reaction, showing that **[1-Cl-F]$_2$** decomposes as the reaction proceeds.

NMR spectra of cyclooctane fluorination with **1-Cl-MeCN** also show presence of free ph$_2$phen ligand within the first five minutes of the reaction. A fluorinated complex could not be observed or isolated in this case. Both **1-Cl-MeCN** and **2** are thus presumed to undergo multiple transitions, including ligand dissociation and fluorination, during the photocatalytic reactions. The isolation of a fluorinated uranyl complex is notable given the calculations performed by Wu *et al.* on cyclooctane fluorination by uranyl nitrate.[4] Fluorine atom abstraction by uranium from the fluorinating agent NFSI was calculated to have a higher activation barrier (15.5 kcal/mol) than HAA from the cyclooctane substrate (10.8 kcal/mol).

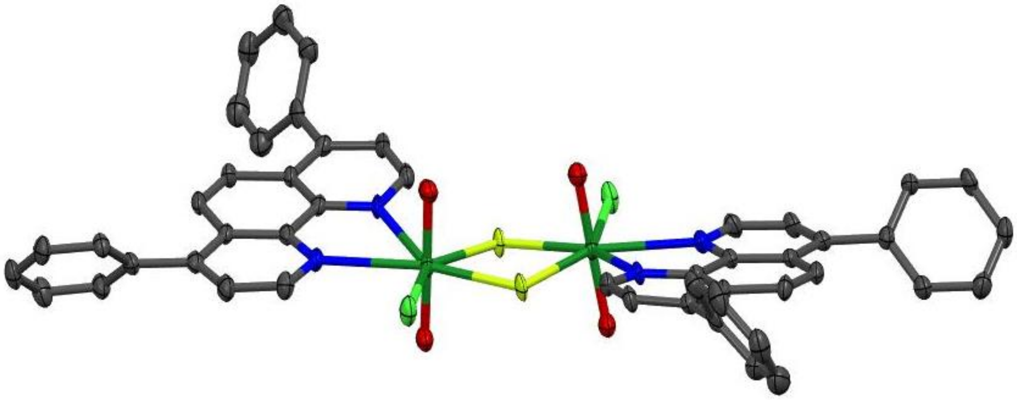

Figure 2.1 Solid-state structure of $[UO_2ClF(ph_2phen)]_2$, **$[1\text{-}Cl\text{-}F]_2$**, with thermal ellipsoids at the 50% probability level. Hydrogen atoms are omitted for clarity. Color code: dark green – U, red – O, light green – Cl, blue – N, grey – C, yellow - F.

The changes in uranyl complexes during the first two hours of fluorination reactions were confirmed by UV/vis spectrophotometry. In the reaction with **1-Cl-MeCN**, the uranyl LMCT absorption peak with its characteristic vibronic coupling structure is observed at *ca*. 400-500 nm at start of the reaction (Figure 2.2, top) This peak could appear due to decomposition of the ph2phen ligand as it is not observed with $[UO_2Cl_2(MeCN)]$ (Figure 2.4). Furthermore, within two hours a more intense peak appears in the region and obscures the uranyl absorption. Furthermore, even after one minute of reaction, the UV/vis spectrum seems to show two overlapping uranyl LMCT peaks, which suggests the presence of two uranyl species, while at ten minutes the absorption peaks match those for $[UO_2Cl_2(MeCN)]$ (Figure 2.2, bottom). This matches the observed free ph_2phen ligand in the NMR spectrum of the reaction in that time range. Assuming that $[UO_2Cl_2(MeCN)]$ remained in solution after two hours of the reaction, its LMCT absorption would still be mostly hindered by the intense absorption in the same region, slowing down photocatalytic activity.

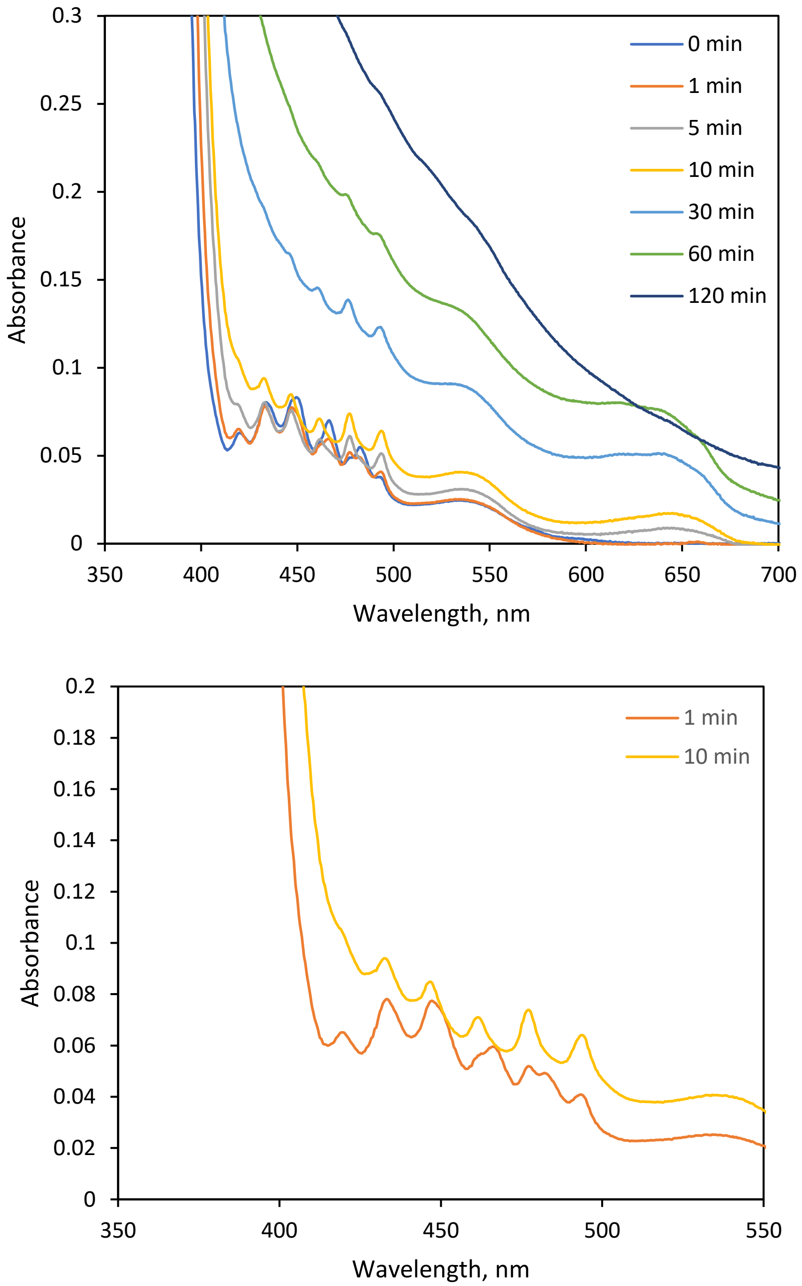

Figure 2.2 Tracking uranyl photocatalyst absorption by UV/vis in cyclooctane fluorination by **1-Cl-MeCN**.

The UV/vis spectra of the reaction with **2** show a similar peak growing in within two hours. Earlier time points for this reaction could not be recorded due to the reaction mixture being cloudy.

UV/vis spectra of the reaction with [UO_2Cl_2(MeCN)] also show a gradual change in the uranyl LMCT absorption.

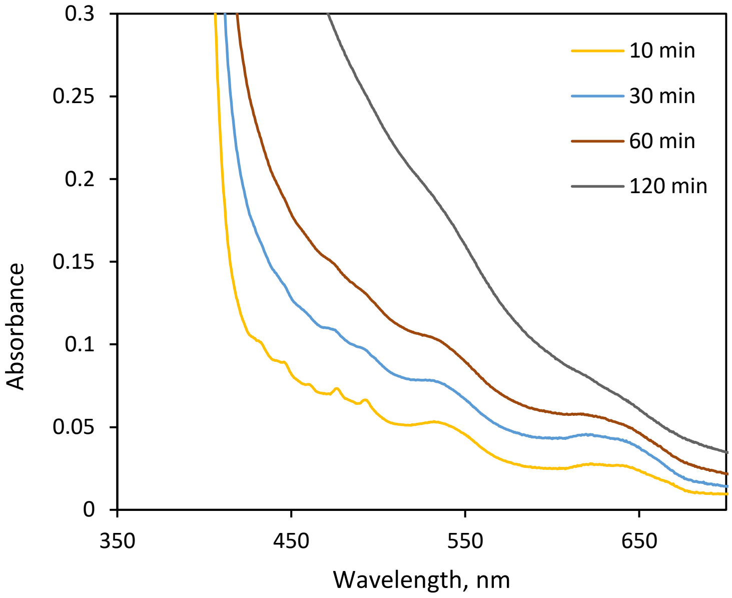

Figure 2.3 Tracking uranyl photocatalyst absorption by UV/vis in cyclooctane fluorination by **2**.

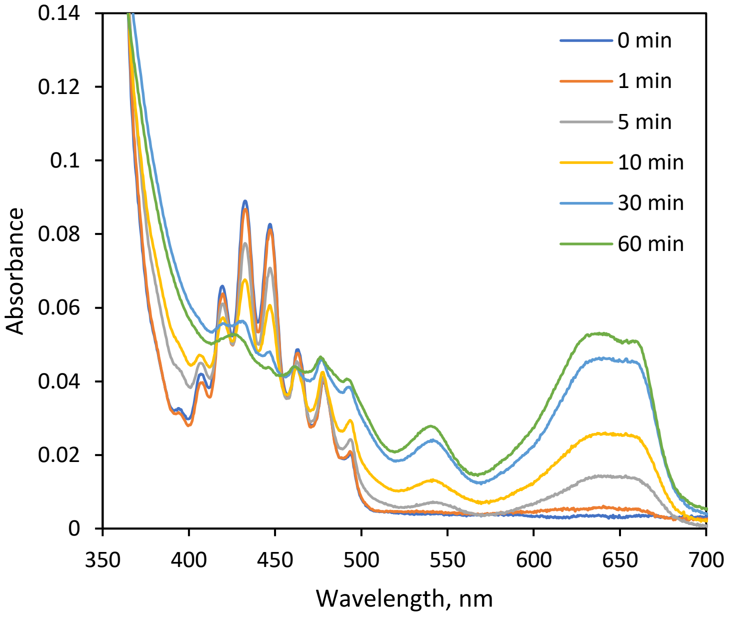

Figure 2.4 Tracking uranyl photocatalyst absorption by UV/vis in cyclooctane fluorination by [UO_2Cl_2(MeCN)].

2.3.2 C-C coupling reactions

The new uranyl complexes were also tested for C-C coupling reactions first reported by Capaldo *et al.*[5], using benzylidene malononitrile as a Michael acceptor. The reactions were carried out under inert atmosphere and the product was quantified by proton NMR. In this case, [UO_2Cl_2(MeCN)] gave the highest yield of product (Table 2.4). In contrast to the fluorination reaction, complex **2** did not dissolve in the reaction mixture and yielded almost no product.

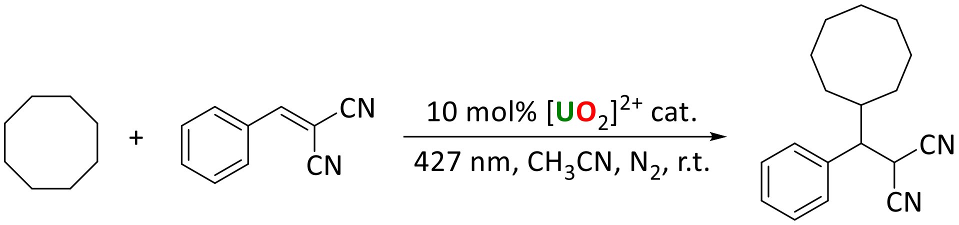

Scheme 2.7 Photocatalytic cyclooctane addition to benzylidene malononitrile.

Table 2.4 Cyclooctane addition to benzylidene malononitrile with different uranyl photocatalysts.

[U] catalyst	**Yield (%)**
[UO_2Cl_2(MeCN)]	21
[UO_2Cl_2(ph_2phen)(MeCN)], **1-Cl-MeCN**	18
[UO_2Cl_2(ph_2phen)$_2$], **2**	Trace product

2.3.3 Oxidation reactions

Uranyl complexes **1-Cl-MeCN** and **2** were also tested for cyclooctane oxidation, and their reactivity compared to the previously reported complex **1-NO$_3$** as well as uranyl nitrate. The reactions were carried out in air so that the carbon-centered radical on the substrate created during the HAA step could be quenched with atmospheric oxygen. The reactions were analyzed by GC. In all cases, the ketone product cyclooctanone was found to be the major product, with smaller amounts of cyclooctanol produced as well. Similar to the fluorination reaction, uranyl nitrate was found to give the highest conversion of cyclooctane, while **1-NO$_3$** gave the second highest yield. For the three uranyl chloride complexes, both ph_2phen-ligated complexes produced slightly higher yields compared to uranyl chloride.

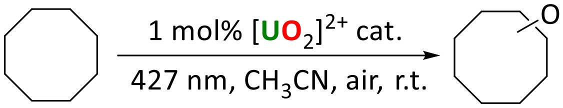

Scheme 2.8 Photocatalytic oxidation of cyclooctane by uranyl complexes.

Table 2.5 Cyclooctane oxidation reactions with different uranyl photocatalysts.

[U] catalyst	**Cyclooctane conversion (%)**
$[UO_2Cl_2(H_2O)_3]$	44
$[UO_2Cl_2(ph_2phen)(MeCN)]$, **1-Cl-MeCN**	52
$[UO_2Cl_2(ph_2phen)_2]$, **2**	49
$[UO_2(NO_3)_2(ph_2phen)]$, **1-NO$_3$**	69
$[UO_2(NO_3)_2(OH_2)_2]\cdot 4H_2O$	80

2.3.4 Computational studies

To further look into the effect of ph_2phen ligand on photocatalytic reactivity of the uranyl ion, reaction activation barriers for hydrogen atom abstraction from cyclooctane were calculated for **1-Cl-MeCN** and $[UO_2Cl_2(MeCN)_3]$ at the scalar−ZORA PBE/TZP level of theory. The energy profiles as well as spin density of reactant, transition state, and product are shown in **Figure 2.5**. The reaction barrier was found to be higher for **1-Cl-MeCN** (8 kcal/mol) than for $[UO_2Cl_2(MeCN)_3]$ (1 kcal/mol). In the reaction with **1-Cl-MeCN**, the spin density is initially on the ph_2phen ligand, but appears to move to the uranyl unit to from an oxyl radical in the transition state.

Interactions between the cyclooctane substrate and the two uranyl complexes were also measured for both ground state (S_0) and excited state (T_1) uranyl complexes as well as transition state (TS) (Table 2.6). In all three cases the ph_2phen ligand was found to be beneficial in forming dispersion interactions with the substrate, showing that incorporation of an organic ligand can be used to attract the substrate to the uranyl catalyst and thus potentially improve photocatalytic reactivity.

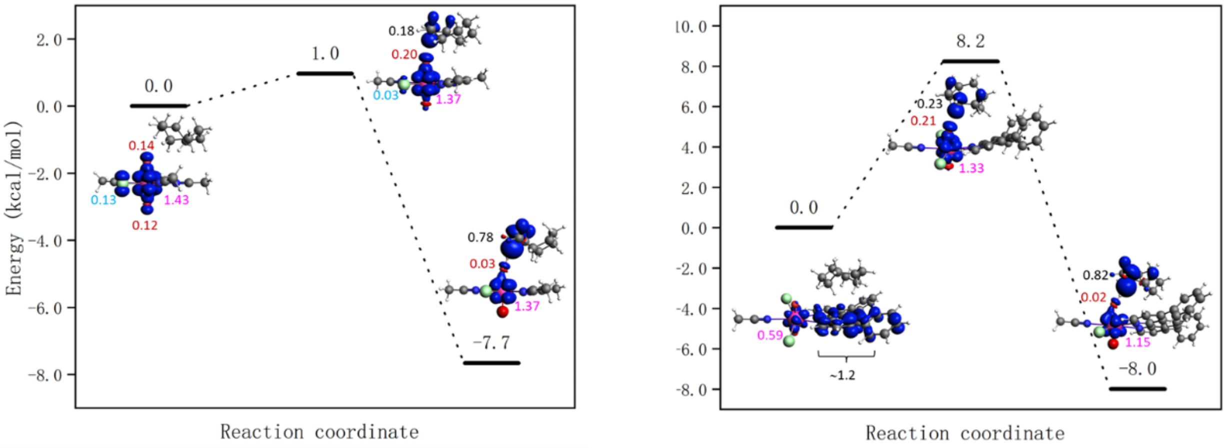

Figure 2.5 Energy profiles for HAA from cyclooctane by the excited state of [$UO_2Cl_2(MeCN)_3$] (left) and **1-Cl-MeCN** (right) calculated at the scalar–ZORA PBE/TZP level of theory. Spin density of reactant, transition state, and product are shown. Color code: pink – U, red – O, light green – Cl, blue – N, grey – C, white - H.

Table 2.6 Dispersion interactions between cyclooctane and uranyl complexes at different stages in kcal/mol calculated at the scalar–ZORA PBE0/TZP level of theory.

	S_0	T_1	TS
[$UO_2Cl_2(MeCN)_3$]	-6.86	-6.60	-6.75
[$UO_2Cl_2(ph_2phen)(MeCN)$]	-11.32	-11.88	-9.49

2.3.5 Stern-Volmer analysis

The photoexcited uranyl(VI) can undergo apparent quenching by both static and dynamic collisional quenching and subsequent electron transfer processes, which would, to a first approximation, result in either productive or unproductive alkane H atom abstraction respectively. Stern-Volmer analyses of [$UO_2Cl_2(MeCN)$] and **2** were carried out in the presence of cyclooctane substrate. The Stern-Volmer equation (Eq. 1) describes the relationship between the concentration of a quenching species and the measured emission intensity.[14]

$$I_0 / I_{[Q]} = 1 + k_q\tau_0 \times [Q] \qquad \textbf{(Eq 1.)}$$

A plot of the emission intensity in the absence of a quenching species (I_0) divided by the observed emission intensity at a given quenching species concentration ($I_{[Q]}$) against the concentration of the quenching species (Q) gives a straight line when there is a single mechanism of quenching with a rate constant that can be determined directly from the slope. When two or more quenching mechanisms are present in a system, the Stern-Volmer plot gives a more complicated function.

Plots of emission intensity and luminescence lifetimes in the absence of substrate (I_0, t_0) and in the presence of increasing amounts of substrate (I, t) in acetonitrile at room temperature are presented in Figures 2.6 and 2.7. Any differences in the change in lifetime *vs*. change in emission intensity can indicate the predominant form of quenching. If there is a change in lifetime upon increasing quencher concentration, quenching is static. If the values $I_0/I = \tau_0/\tau$ then only dynamic quenching is occurring.

Monitoring the emission intensity lifetimes of the uranyl(VI) band for **2** at 522 nm following equilibration after successive addition of 1mL aliquots of cyclooctane (0 – 50 mM) applying a 50 ms time delay affords a positive Stern-Volmer relationship in both the intensity and lifetime plots, with a quenching constant, K_{SV} of 1074. However, the slopes of the plots of $I_0/I = \tau_0/\tau$ are not identical; that for I_0/I is a magnitude greater than for τ_0/τ. This suggests that a combination of both static and dynamic quenching mechanisms are operative for **2** with the cyclooctane substrate.

The same Stern-Volmer analysis of $[UO_2Cl_2(MeCN)]$ with cyclooctane (Figure 2.8) also shows a linear relationship with respect to emission lifetime and intensity (monitored at 510 nm) but the K_{SV} value (383) is approximately three times smaller, and in this case I_0/I is closer in value τ_0/τ, which indicates that dynamic quenching processes contribute more to the excited state chemistry in this system than in **2**. This suggests that **2** is a better catalyst than $[UO_2Cl_2(MeCN)]$. Stern-Volmer measurements for **1-Cl-MeCN** for comparison are in progress.

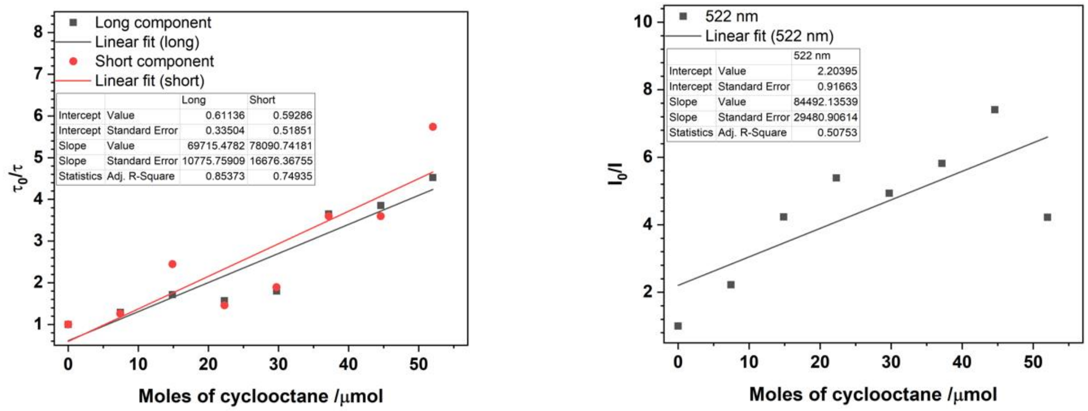

		Long	Short
Intercept	Value	0.61136	0.59286
Intercept	Standard Error	0.33504	0.51851
Slope	Value	69715.4782	78090.74181
Slope	Standard Error	10775.75909	16676.36755
Statistics	Adj. R-Square	0.85373	0.74935

		522 nm
Intercept	Value	2.20395
Intercept	Standard Error	0.91663
Slope	Value	84492.13539
Slope	Standard Error	29480.90614
Statistics	Adj. R-Square	0.50753

Figure 2.6 Stern-Volmer plots for samples of $[UO_2Cl_2(ph_2phen)_2]$ (**2**), comparing the luminescence lifetimes (left) and intensities (right) with increasing amounts of cyclooctane based on three sets of measurements. Estimated error ± 10%.

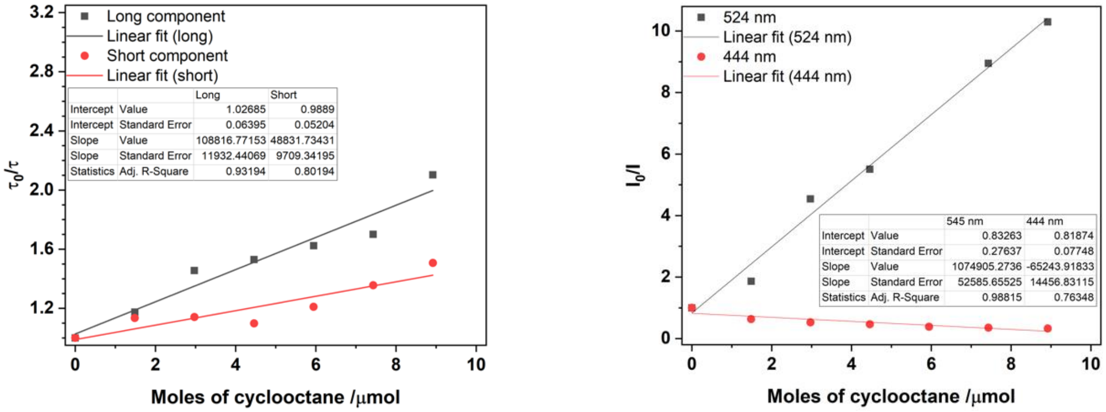

Figure 2.7 Stern-Volmer plots for samples of [$UO_2(ph_2phen)_2$] (**2**), comparing the luminescence lifetimes (left) and intensities (right) with increasing amounts of cyclooctane with a 50 µs time gate applied. Estimated error ± 10%.

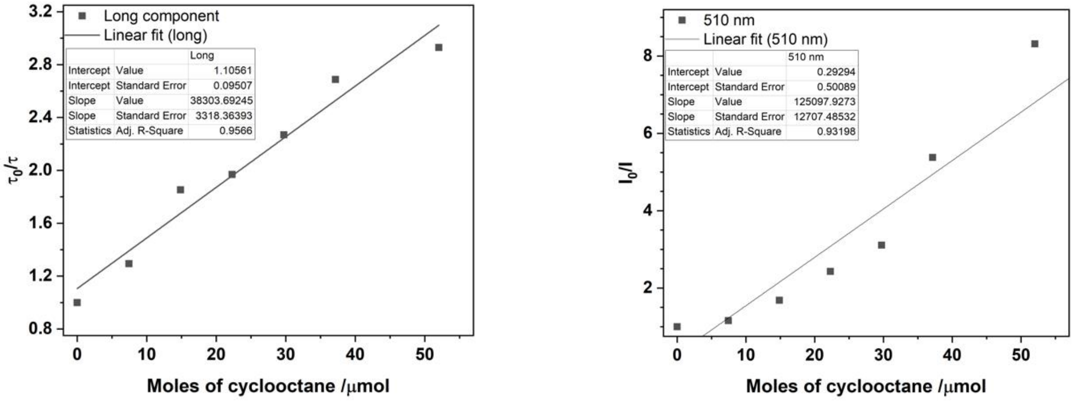

Figure 2.8 Stern-Volmer plots for samples of [$UO_2Cl_2(MeCN)$] comparing the luminescence lifetimes (left) and intensities (right) with increasing amounts of cyclooctane.

2.4 Conclusion

The new uranyl chloride ph_2phen complexes were tested in photocatalytic fluorination, oxidation and C-C coupling reactions with cyclooctane as a model substrate with a strong C-H bond. In fluorination reactions, the ph_2phen complexes **1-Cl-MeCN** and **2** were both found to form other uranyl species as the reaction progressed. A fluorinated uranyl complex **[1-Cl-F]₂** was isolated, showing that the fluorinating agent NFSI was capable of fluorinating the uranyl precatalyst or catalyst. Regardless, the presence of ph_2phen was found to increase the yield of fluorocyclooctane. While uranyl nitrate was found to be a superior catalyst in both fluorination and oxidation reactions, DFT calculations and Stern-Volmer analyses show that an organic ligand can nevertheless be beneficial to photocatalysis.

2.5 Experimental details

Solvents and reagents. Chemicals and solvents were purchased from Sigma Aldrich or Fisher Scientific. Deuterated solvents were purchased from Cambridge Isotope Laboratories. Solids used for anaerobic reactions (uranyl complexes, *N*-fluorobenzenesulfonimide) were dried under vacuum on a high-vacuum Schlenk-line overnight before use. Cyclooctane was freeze-pump-thaw degassed three times and stored over 3 Å molecular sieves under an N_2 atmosphere for one week before use. Acetonitrile was dried using an MBRAUN SPS 800 Manual solvent purification system and stored over activated 3 Å molecular sieves. CD_3CN was dried over calcium hydride before being freeze-pump-thaw degassed three times and purified by trap-to-trap distillation. **1-NO$_3$** was synthesized according to a literature procedure.[9] Complexes [UO_2Cl_2(MeCN)], **1-Cl-MeCN** and **2** were prepared as described in Chapter 1.

General procedure for photocatalytic fluorination of cyclooctane. All the reactions were performed in a nitrogen-atmosphere glovebox. A mixture of cyclooctane (81 µL, 6 x 10^{-4} mol, 0.6 M), NFSI (283.8 mg, 6 x 10^{-4} mol) and uranyl catalyst (1 mol%, 6.0 x 10^{-6} mol, 6.0 x 10^{-3} M) in acetonitrile (1 mL) was added to a 20 mL borosilicate glass vial and the solution magnetically stirred 5 cm away from a 427 nm LED lamp (Kessil PR160L 427) at ~100 rpm for 16 h. An internal standard (methyl acetate, 20 µL) was then added to an aliquot of the reaction mixture (0.4 µL) and the ^{1}H and ^{19}F NMR spectrum of the solution was recorded. The yield of fluorocyclooctane was calculated by comparing the integral of the doublet at 4.64 ppm (*J* = 46.4 Hz, 1H) to methyl acetate peak (3.67 – 3.45 ppm, m, 3H).

Photocatalytic oxidation. A mixture of cyclooctane (81 µL, 6 x 10^{-4} mol, 0.6 M) and uranyl catalyst (1 mol%, 6.0 x 10^{-6} mol, 6.0 x 10^{-3} M) in acetonitrile (1 mL) was added to a 20 mL borosilicate glass vial with a pierced lid and the solution magnetically stirred 5 cm away from a 427 nm LED lamp (Kessil PR160L 427) at ~100 rpm for 16 h. The reaction mixture was then analyzed by gas chromatography with dodecane as internal standard.

C-C coupling reactions. All the reactions were performed in a nitrogen-atmosphere glovebox. A mixture of cyclooctane (81 µL, 6 x 10^{-4} mol, 0.6 M), benzylidene malononitrile (92.5 mg, 6 x 10^{-4} mol) and uranyl catalyst (1 mol%, 6.0 x 10^{-6} mol, 6.0 x 10^{-3} M) in acetonitrile (1 mL) was added to a 20 mL borosilicate glass vial and the solution magnetically stirred 5 cm away from a 427 nm LED lamp (Kessil PR160L 427) at ~100 rpm for 16 h. An internal standard (methyl acetate, 20 µL) was then added to an aliquot of the reaction mixture (0.4 µL) and the ^{1}H and ^{19}F NMR spectrum of the solution was recorded. The yield of fluorocyclooctane was calculated by comparing the integral of the doublet at 4.58 ppm (*J* = 5.8 Hz, 1H) to methyl acetate peak (3.67 – 3.45 ppm, 3H).

Characterization. NMR spectra were recorded on Bruker Avance 400 MHz spectrometers and are referenced to residual protio solvent (1.94 ppm for MeCN-d_3,) for ^{1}H NMR spectroscopy. Acetonitrile was used as solvent for no-deuterium NMR experiments and was referenced to the solvent peak (1.94 ppm). Chemical shifts are quoted in ppm and coupling constants in Hz. NMR spectra were taken at 25°C. UV/vis spectra of anaerobic reactions were collected using quartz cells with a 10 mm pathlength equipped with a J-Young valve with samples prepared under a dinitrogen atmosphere. GC analyses and calibration curves were obtained on an Agilent 6890 GC equipped with an HP-5 column (25 m x 0.20 mm ID x 0.33 m film) and an FID detector.

Crystallography. X-ray diffraction data for **[1-Cl-F]$_2$** were collected at beamline 12.2.1 of the Advanced Light Source (ALS) at Lawrence Berkeley National Lab, using a Bruker D8 diffractometer coupled to a Bruker PhotonII CPAD detector with Si(111)-monochromated synchrotron radiation (17 keV radiation). Absorption corrections were completed using APEX III software. All structures were solved using SHELXT in Olex2 and refined using SHELXL in Olex2.[15,16] Analytical numeric absorption corrections used a multifaceted crystal model based on expressions derived by Clark and Reid.[17] Numerical absorption correction was based on a Gaussian integration over a multifaceted crystal model. All non-hydrogen atoms were refined with anisotropic displacement parameters and H-parameters were constrained to parent atoms and refined using a riding model.

Computational details. Unless specified, all calculations were carried out using the ADF 2021 software package,[18,19] the PBE[20] and PBE0[21,22] functional with a scalar relativistic ZORA Hamiltonian,[23–25] and the small frozen core TZP basis set for all elements.[26] All geometry optimizations were carried out in conjunction with the COSMO[27] implicit solvation model. The radii values of the atomic spheres in the COSMO solvation model for atoms in this study are the corresponding van der Waals radii from the MM3 method by Allinger[28] divided by 1.2. We note that the heavy uranium metal is well buried inside of the first solvation shell and does not have direct contact with the solvation cavity. Hence, its radius setting does not affect the results of the geometry optimization. The spin-orbit coupling effect was not considered in this work as, for the types of compounds studied here, it has only a minor effect on molecular structures, vibrational frequencies, and reaction energies. Grimme's D3 dispersion[29] correction with Becke-Johnson damping (D3BJ)[30] was used for the actinyl systems. Frequency calculations were performed to ensure optimization convergence to local minima and transition states on the potential energy surface. Finally, in order to obtain higher accuracy energies in HAT reaction, single point energy correction at coupled cluster level (DLPNO-CCSD(T))[31] on the solution-optimized geometries from ADF PBE0 level were carried on using ORCA code.[32] Scalar relativistic effects were included with the ZORA Hamiltonian and the corresponding basis set ZORA-def2-TZVP.[33]

Stern-Volmer analysis. An optically dilute solution (absorbance at the excitation emission wavelength ~0.1) of each compound in analytical grade MeCN was prepared. The emission spectrum and luminescence lifetimes of the emission bands (in the absence of any quencher) and then upon increasing additions 0.2 uL aliquots of cyclooctane (0.2 - 1.2 µL) were recorded following indirect excitation at 280 nm and direct uranyl LMCT excitation at 427 nm and 440 nm. Spectra were recorded on an Edinburgh Instruments FP920 Phosphorescence Lifetime Spectrometer equipped with a 450 W steady state xenon lamp, a 5 W microsecond pulsed xenon flashlamp, with single 300 mm focal length excitation and emission monochromators in Czerny Turner configuration, and a red sensitive photomultiplier in Peltier (air cooled) housing (Hamamatsu R928P).

Data were analyzed according to the Stern-Volmer model (Eq. 1) where I is the initial UO_2^{2+} emission intensity before addition of the quencher, Q (cyclooctane), I_0 is fluorescence intensity in the presence of a quencher; K_{SV} is the Stern Volmer quenching constant Q is derived from the gradient of the slope of I_0/I *vs.* [Q] or τ_0/τ *vs*. [Q].

$$I/I_0 \text{ or } \tau/\tau_0 = 1 + K_{SV}[Q]$$ **Equation 1**

Table 2.7 Crystal data and structure refinement for **[1-Cl-F]$_2$**

Complex	**[1-Cl-F]$_2$**
Empirical formula	$C_{48}H_{32}Cl_2F_2N_4O_4U_2$
Formula weight	1313.73
Temperature/K	100
Crystal system	orthorhombic
Space group	*Pnna*
a/Å	15.7599(16)
b/Å	17.6063(16)
c/Å	15.3755(14)
α/°	90
β/°	90
γ/°	90
Volume/Å^3	4266.3(7)
Z	4
ρ_{calc} g/cm^3	2.045
μ/mm^{-1}	3.663
F(000)	2464.0
Crystal size/mm^3	0.13 × 0.13 × 0.12
Radiation	synchrotron (λ = 0.7288)
2Θ range for data collection/°	3.606 to 54.376
Index ranges	$-19 \leq h \leq 19$, $-22 \leq k \leq 22$, $-19 \leq l \leq 19$
Reflections collected	87318
Independent reflections	4407 [R_{int} = 0.0854, R_{sigma} = 0.0316]
Data/restraints/parameters	4407/0/280
Goodness-of-fit on F^2	1.032
Final R indexes [I>=2σ (I)]	R_1 = 0.0279, wR_2 = 0.0584
Final R indexes [all data]	R_1 = 0.0394, wR_2 = 0.0625
Largest diff. peak/hole / e Å^{-3}	1.41/-0.94

2.6 References

(1) Blanksby, S. J.; Ellison, G. B. Bond Dissociation Energies of Organic Molecules. *Acc Chem Res* **2003**, *36* (4), 255–263. https://doi.org/10.1021/ar020230d.

(2) Capaldo, L.; Quadri, L. L.; Ravelli, D. Photocatalytic Hydrogen Atom Transfer: The Philosopher's Stone for Late-Stage Functionalization? *Green Chemistry*. Royal Society of Chemistry June 7, 2020, pp 3376–3396. https://doi.org/10.1039/d0gc01035a.

(3) West, J. G.; Bedell, T. A.; Sorensen, E. J. The Uranyl Cation as a Visible-Light Photocatalyst for C(Sp ^{3})−H Fluorination. *Angewandte Chemie International Edition* **2016**, *55* (31), 8923–8927. https://doi.org/10.1002/anie.201603149.

(4) Wu, L.; Cao, X.; Chen, X.; Fang, W.; Dolg, M. Visible-Light Photocatalysis of C(Sp3)-H Fluorination by the Uranyl:Mechanistic Insights. *Angewandte Chemie* **2018**, *130* (36), 11986–11990. https://doi.org/10.1002/ange.201806554.

(5) Capaldo, L.; Merli, D.; Fagnoni, M.; Ravelli, D. Visible Light Uranyl Photocatalysis: Direct C-H to C-C Bond Conversion. *ACS Catal* **2019**, *9* (4), 3054–3058. https://doi.org/10.1021/acscatal.9b00287.

(6) Yu, J.; Zhao, C.; Zhou, R.; Gao, W.; Wang, S.; Liu, K.; Chen, S.; Hu, K.; Mei, L.; Yuan, L.; Chai, Z.; Hu, H.; Shi, W. Visible-Light-Enabled C−H Functionalization by a Direct Hydrogen Atom Transfer Uranyl Photocatalyst. *Chemistry - A European Journal* **2020**, *26* (69), 16521–16529. https://doi.org/10.1002/chem.202003431.

(7) Azam, M.; Al-Resayes, S. I.; Trzesowska-Kruszynska, A.; Kruszynski, R.; Kumar, P.; Jain, S. L. Seven-Coordinated Chiral Uranyl(VI) Salen Complex as Effective Catalyst for C–H Bond Activation of Dialkylanilines under Visible Light. *Polyhedron* **2017**, *124*, 177–183. https://doi.org/10.1016/j.poly.2016.12.033.

(8) Mashita, T.; Tsushima, S.; Takao, K. Photocatalytic Oxygenation of Cyclohexene Initiated by Excitation of [UO2(OPCyPh2)4] 2+ under Visible Light. *ACS Omega* **2019**, *4* (4), 7194–7199. https://doi.org/10.1021/acsomega.9b00635.

(9) Arnold, P. L.; Purkis, J. M.; Rutkauskaite, R.; Kovacs, D.; Love, J. B.; Austin, J. Controlled Photocatalytic Hydrocarbon Oxidation by Uranyl Complexes. *ChemCatChem* **2019**, *11* (16), 3786–3790. https://doi.org/10.1002/cctc.201900037.

(10) Sarakha, M.; Bolte, M.; Burrows, H. D. *The Photo-Oxidation of 2,6-Dimethylphenol and Monophenylphenols by Uranyl Ion in Aqueous Solution*; 1997; Vol. 07.

(11) Li, Y.; Rizvi, S. A.; Hu, D.; Sun, D.; Gao, A.; Zhou, Y.; Li, J.; Jiang, X. Selective Late-Stage Oxygenation of Sulfides with Ground-State Oxygen by Uranyl Photocatalysis. *Angewandte Chemie* **2019**, *131* (38), 13633–13640. https://doi.org/10.1002/ange.201906080.

(12) Burrows, H. D.; Kemp, T. J. The Photochemistry of the Uranyl Ion. *Chem Soc Rev* **1974**, No. 3, 139–165.

(13) Luo, Y.-R. *Comprehensive Handbook of Chemical Bond Energies*; Taylor & Francis Group, LLC, 2007.

(14) Lakowicz, J. R. *Principles of Fluorescence Spectroscopy*, 3rd ed.; Springer: New York, NY, 2006.

(15) Dolomanov, O. V; Bourhis, L. J.; Gildea, R. J.; Howard, J. A. K.; Puschmann, H. OLEX2: A Complete Structure Solution, Refinement and Analysis Program. *J Appl Crystallogr* **2009**, *42* (2), 339–341. https://doi.org/10.1107/S0021889808042726.

(16) Sheldrick, G. M. SHELXT – Integrated Space-Group and Crystal-Structure Determination. *Acta Crystallographica Section A* **2015**, *71* (1), 3–8. https://doi.org/10.1107/S2053273314026370.

(17) Clark, R. C.; Reid, J. S. The Analytical Calculation of Absorption in Multifaceted Crystals. *Acta Crystallographica Section A* **1995**, *51* (6), 887–897. https://doi.org/10.1107/S0108767395007367.

(18) te Velde, G.; Bickelhaupt, F. M.; Baerends, E. J.; Fonseca Guerra, C.; van Gisbergen, S. J. A.; Snijders, J. G.; Ziegler, T. Chemistry with ADF. *J Comput Chem* **2001**, *22* (9), 931–967. https://doi.org/10.1002/jcc.1056.

(19) ADF . SCM, Theoretical Chemistry, Vrije Universiteit, Amsterdam, The Netherlands. . http://www.scm.com/. (accessed 2023-07-28).

(20) Perdew, J. P.; Burke, K.; Ernzerhof, M. *Generalized Gradient Approximation Made Simple*; 1996.

(21) Perdew, J. P.; Ernzerhof, M.; Burke, K. Rationale for Mixing Exact Exchange with Density Functional Approximations. *Journal of Chemical Physics* **1996**, *105* (22), 9982–9985. https://doi.org/10.1063/1.472933.

(22) Adamo, C.; Barone, V. Toward Reliable Density Functional Methods without Adjustable Parameters: The PBE0 Model. *Journal of Chemical Physics* **1999**, *110* (13), 6158–6170. https://doi.org/10.1063/1.478522.

(23) Van Lenthe, E.; Baerends, E. J.; Snijders, J. G. Relativistic Regular Two-Component Hamiltonians. *J Chem Phys* **1993**, *99* (6), 4597–4610. https://doi.org/10.1063/1.466059.

(24) Van Lenthe, E.; Baerends, E. J.; Snijders, J. G. Relativistic Total Energy Using Regular Approximations. *J Chem Phys* **1994**, *101* (11), 9783–9792. https://doi.org/10.1063/1.467943.

(25) Van Lenthe, E. Geometry Optimizations in the Zero Order Regular Approximation for Relativistic Effects. *Journal of Chemical Physics* **1999**, *110* (18), 8943–8953. https://doi.org/10.1063/1.478813.

(26) Van Lenthe, E.; Baerends, E. J. Optimized Slater-Type Basis Sets for the Elements 1-118. *J Comput Chem* **2003**, *24* (9), 1142–1156. https://doi.org/10.1002/jcc.10255.

(27) Pye, C.; Ziegler, T.; Lenthe, E.; Louwen, J. An Implementation of the Conductor-like Screening Model of Solvation within the Amsterdam Density Functional Package — Part II. COSMO for Real Solvents1. *Can J Chem* **2009**, *87*, 790–797. https://doi.org/10.1139/V09-008.

(28) Allinger, N. L.; Zhou, X.-Z.; Bergsma, J. S. Molecular Mechanics Parameters. *Journal of Molecular Structure-theochem* **1994**, *312*, 69–83.

(29) Grimme, S.; Antony, J.; Ehrlich, S.; Krieg, H. A Consistent and Accurate Ab Initio Parametrization of Density Functional Dispersion Correction (DFT-D) for the 94 Elements H-Pu. *Journal of Chemical Physics* **2010**, *132* (15). https://doi.org/10.1063/1.3382344.

(30) Grimme, S.; Ehrlich, S.; Goerigk, L. Effect of the Damping Function in Dispersion Corrected Density Functional Theory. *J Comput Chem* **2011**, *32* (7), 1456–1465. https://doi.org/10.1002/jcc.21759.

(31) Paulechka, E.; Kazakov, A. Efficient DLPNO-CCSD(T)-Based Estimation of Formation Enthalpies for C-, H-, O-, and N-Containing Closed-Shell Compounds Validated Against Critically Evaluated Experimental Data. *Journal of Physical Chemistry A* **2017**, *121* (22), 4379–4387. https://doi.org/10.1021/acs.jpca.7b03195.

(32) Neese, F. Software Update: The ORCA Program System, Version 4.0. *Wiley Interdiscip Rev Comput Mol Sci* **2018**, *8* (1). https://doi.org/10.1002/wcms.1327.

(33) Weigend, F.; Ahlrichs, R. Balanced Basis Sets of Split Valence, Triple Zeta Valence and Quadruple Zeta Valence Quality for H to Rn: Design and Assessment of Accuracy. *Physical Chemistry Chemical Physics* **2005**, *7* (18), 3297–3305. https://doi.org/10.1039/b508541a.